

1 **A globally distributed dataset of coseismic**  
2 **landslide mapping via multi-source high-resolution**  
3 **remote sensing images**

4 Chengyong Fang<sup>1</sup>, Xuanmei Fan<sup>1\*</sup>, Xin Wang<sup>1</sup>, Lorenzo Nava<sup>2</sup>, Hao Zhong<sup>1,3</sup>, Xiujun Dong<sup>1</sup>,  
5 Jixiao Qi<sup>1</sup>, Filippo Catani<sup>2</sup>

6 <sup>1</sup>State Key Laboratory of Geohazard Prevention and Geoenvironment Protection, Chengdu  
7 University of Technology, 610059, Chengdu, China

8 <sup>2</sup>Machine Intelligence and Slope Stability Laboratory, Department of Geosciences, University  
9 of Padua, 35129 Padua, Italy

10 <sup>3</sup>College of Information Science and Technology, Chengdu University of Technology, 610059,  
11 Chengdu, China

12 *Correspondence to:* Xuanmei Fan ([fxm\\_cdut@qq.com](mailto:fxm_cdut@qq.com))

13

14

## 15 Abstract

16 Rapid and accurate mapping of landslides triggered by extreme events is essential for  
17 effective emergency response, hazard mitigation, and disaster management. However, the  
18 development of generalized machine learning models for landslide detection has been hindered  
19 by the absence of a high-resolution, globally distributed, event-based dataset. To address this  
20 gap, we introduce the Globally Distributed Coseismic Landslide Dataset (GDCLD), a  
21 comprehensive dataset that integrates multi-source remote sensing images, including  
22 PlanetScope, Gaofen-6, Map World, and Unmanned Aerial Vehicle data, with varying  
23 geographical and geological background for nine events across the globe. In this study, we  
24 evaluated the effectiveness of GDCLD by comparing the mapping performance of seven state-  
25 of-the-art semantic segmentation algorithms. These models were further tested by three  
26 different types of remote sensing images in four independent regions, while the GDCLD-  
27 SegFormer model get the best performance. Additionally, we extended the evaluation to a  
28 rainfall-induced landslide dataset, where the models demonstrated excellent performance as  
29 well, highlighting the dataset's applicability to landslide segmentation triggered by other factors.  
30 Our results confirm the superiority of GDCLD in remote sensing landslide detection modeling,  
31 offering a comprehensive data base for rapid landslide assessment following future unexpected  
32 events worldwide.

33

34

# 35 1. Introduction

36 Landslides triggered by extreme events such as earthquakes and heavy precipitation are  
37 responsible for most of the damage to mountainous settlements (Huang and Fan, 2013). In  
38 some cases, landslides can be even more disastrous than the triggering events themselves, as  
39 they can render emergency responses ineffective by cutting off roads and other transportation  
40 lifelines (Cigna et al., 2012; Huang et al., 2012; Valagussa et al., 2019; Chau et al., 2004).  
41 Therefore, the rapid and accurate identification of landslides after extreme events is crucial for  
42 timely and quantitative assessment of disasters. This is especially important for emergency  
43 rescue operations and subsequent risk management in mountainous areas with complex  
44 environments and possibly inconvenient transportation routes. (Cigna et al., 2018; Chau et al.,  
45 2004; Gorum et al., 2011).

46 Conventional landslide mapping efforts rely on traditional surveying methods such as  
47 topographic total stations, field observations to collect essential data on slope stability and  
48 terrain morphology (Brardinoni et al., 2003; Coe et al., 2003; Zhong et al., 2020). These  
49 methods may not capture the full extent of terrain dynamics due to their static nature  
50 (Metternicht et al., 2005). Consequently, these methods are not effective for detailed landslide  
51 mapping, especially when traversing the affected and unstable regions for field surveys is not  
52 possible. This was particularly true for the Wenchuan co-seismic landslides, which mobilized  
53 large amounts of material that obstructed roads, complicating disaster response efforts as well  
54 as surveying and mapping activities (Gorum et al., 2011). With the development of remote  
55 sensing technology in the past decades, landslide investigation has been supported by digital  
56 mapping, which reduces time and labor costs (Fiorucci et al., 2011; Fiorucci et al., 2019; Gao  
57 and Maro, 2010; Guzzetti et al., 2012). This mapping has also been enhanced by various  
58 modalities of sensors, such as synthetic aperture radar (Mondini et al., 2021; Nava et al., 2021),  
59 multi-spectral (Udin et al., 2019), and hyper-spectral (Ye et al., 2019). However, visual  
60 identification is highly subjective due to operator experience, and the interpretation of events  
61 involving numerous landslides is still time-consuming. Therefore, this subjectivity and the time-

62 consuming nature of interpretation hinder the reliability and efficiency of landslide mapping, **for**  
63 **example**, after major events such as the Wenchuan, China (2008), and Gorkha, Nepal (2015)  
64 earthquakes.

65 Generally, the ideal solution is to develop automated models or tools that can save time  
66 and costs while ensuring an objective protocol in the mapping process (Casagli et al., 2023).  
67 While some researchers have endeavored to employ machine learning or deep learning in  
68 constructing these models, most of them lack the generalization capability for application across  
69 diverse environmental backgrounds and remote sensing images (Burrows et al., 2019; Bhuyan  
70 et al., 2023; Li et al., 2016; Liu et al., 2022; Lu et al., 2019; Luppino et al., 2022; Meena et al.,  
71 2021; Soares et al., 2022; Yang et al., 2022a; Mohan et al., 2021; Ss and Shaji, 2022; Li et al.,  
72 2024). To improve such models, more abundant data that consider the diverse  
73 geomorphological and climatic settings where landslides occur are essential. The Bijie landslide  
74 dataset, based on Map World image, presents a small-scale dataset of mountainous landslides,  
75 filling the gap in landslide detection tasks for the first time (Ji et al., 2020). Landslide4sense,  
76 based on Sentinel-2 image, introduces a multispectral landslide dataset, pioneering semantic-  
77 level annotation of landslides (Ghorbanzadeh et al., 2022). The HRGLDD and GVLM datasets,  
78 based on PlanetScope and Google Earth image respectively, propose global-scale high-  
79 resolution landslide datasets (Meena et al., 2022; Zhang et al., 2023). However, these datasets  
80 are limited by their reliance on single remote sensing data sources, restricting the applicability  
81 of models across different sensors and resolutions. The CAS dataset introduces a mountain  
82 landslide dataset containing various remote sensing data sources (Xu et al., 2024). However,  
83 due to its limited annotated landslide quantity, high image overlap, and lack of negative samples  
84 (background/non-landslide), it is still insufficient to effectively generalize to landslide automatic  
85 mapping tasks in various complex environments especially where signatures of landslides often  
86 resemble nearby terrain.

87 **Therefore, there is an urgent need to develop a carefully curated and diverse dataset.** Such  
88 a dataset would facilitate the rapid and accurate mapping of landslides using available prior  
89 knowledge. Hence, we present a comprehensive landslide dataset derived from nine

90 earthquake-triggered landslide **events**, encompassing multi-sensor images from 3m-  
91 PlanetScope, 2m-Gaofen-6, 0.5m-Map World, and 0.2m-UAV. This work addresses the  
92 shortcomings of existing datasets in terms of accuracy and generalization for training large and  
93 complex deep-learning models. It is of great significance for accurate, rapid, and automatic  
94 mapping of landslides occurring anywhere in the world, providing strong support for efficient  
95 geohazard emergency response and investigation.

96 **The paper is structured as follows: Section 2 reviews existing high-quality landslide**  
97 **datasets to provide an overview of the current state of research. Section 3 introduces the data**  
98 **collection and preparation process to showcase the extensive research events and scientific**  
99 **methodology behind our data production. Section 4 describes the semantic segmentation**  
100 **algorithms, loss functions, and parameter settings used in this study, and shows their rationality.**  
101 **Section 5 presents the results, including the training, validation, and testing outcomes of the**  
102 **dataset, as well as the generalization ability of the GDCLD trained model in independent**  
103 **regions. Section 6 discusses the innovation and effectiveness of GDCLD, illustrating its**  
104 **effective application in several landslide events.**

## 105 2. Related work

106 **The most effective approach for landslide mapping currently involves image segmentation,**  
107 **and computer vision segmentation tasks depend heavily on high-quality data to build accurate**  
108 **models. However, landslide segmentation tasks have developed relatively recently compared**  
109 **to other computer vision applications, resulting in only a limited number of studies that have**  
110 **constructed datasets for various landslide events. In this section, we review some of these**  
111 **landslide segmentation datasets and provide detailed information on each (Table.1).**

112 **The Bijie landslide dataset comprises high-resolution satellite images captured in**  
113 **landslide-prone areas of Guizhou province, China. The dataset includes 770 landslide samples**  
114 **and 2,003 non-landslide samples. The positive samples consist of rockfalls, rockslides, and a**  
115 **small number of debris avalanches, while the negative samples include mountains, villages,**  
116 **roads, rivers, and farmland, among others. The image resolutions vary from 61×61 pixels to**

117 1,239×1,197 pixels, with RGB channels. There is a total of  $7.23 \times 10^6$  pixels assigned for  
118 landslide within the dataset (Ji et al., 2020).

119 The landslide4sense dataset consists of multispectral satellite images captured across four  
120 distinct regions. This dataset comprises 3,799 images, each with dimensions of 64×64 pixels  
121 and a spatial resolution of 10 meters. Each image contains 14 bands, including 12 bands from  
122 the Sentinel-2 satellite and 2 bands from Digital Elevation Model (DEM) data. The dataset  
123 includes negative background samples such as bare soil, rivers, and buildings. There is a total  
124 of  $1.76 \times 10^6$  pixels assigned for landslide within the dataset (Ghorbanzadeh et al., 2022).

125 The HR-GLDD spans 10 distinct geographic regions, capturing landslide instances across  
126 various geographical environments in South Asia, Southeast Asia, East Asia, South America,  
127 and Central America. HR-GLDD comprises a total of 1,756 image patches, each standardized  
128 to a size of 128×128 pixels with a spatial resolution of up to 3 meters. The dataset is sourced  
129 from four spectral bands of the PlanetScope satellite. It includes a variety of negative samples,  
130 such as non-landslide terrain features, buildings, and roads, ensuring a comprehensive  
131 representation for model training. There is a total of  $2.96 \times 10^6$  pixels assigned for landslide  
132 within the dataset (Meena et al., 2022).

133 The GVLM dataset spans across six continents and 17 different landslide sites, GVLM  
134 covers a diverse range of geological and climatic conditions, from the lush landscapes of Asia  
135 to the rugged terrain of South America. Comprising 17 pairs of dual-temporal VHR images,  
136 each image pair boasts a spatial resolution of 0.59 meters, ensuring detailed capture of  
137 landslide features and their surrounding environments. GVLM incorporates various negative  
138 samples, including non-landslide landforms, infrastructure such as buildings, and transportation  
139 networks, providing a holistic training ground for models. Image sizes within the GVLM dataset  
140 range from 1,861×1,749 pixels to 10,828×7,424 pixels. There is a total of  $3.24 \times 10^7$  pixels  
141 assigned for landslide within the dataset (Zhang et al., 2023).

142 The CAS Landslide Dataset covers nine different geographic regions spanning South Asia,  
143 Southeast Asia, East Asia, South America, and Central America. Comprising 20,865 image  
144 patches, each standardized to a size of 512×512 pixels, the dataset offers a spatial resolution

145 ranging from 0.2 to 5 meters. During the cropping process, an overlap setting parameter of 0.5  
 146 was used. These images are sourced from unmanned aerial vehicles (UAVs) and satellite  
 147 platforms, integrating data from the PlanetScope satellite and other sources. The dataset  
 148 removes background images that do not contain landslide pixels and therefore lacks sufficient  
 149 background noise as negative samples to enhance the robustness of the model. There is a total  
 150 of  $1.95 \times 10^8$  pixels assigned for landslide within the dataset (Xu et al., 2024).

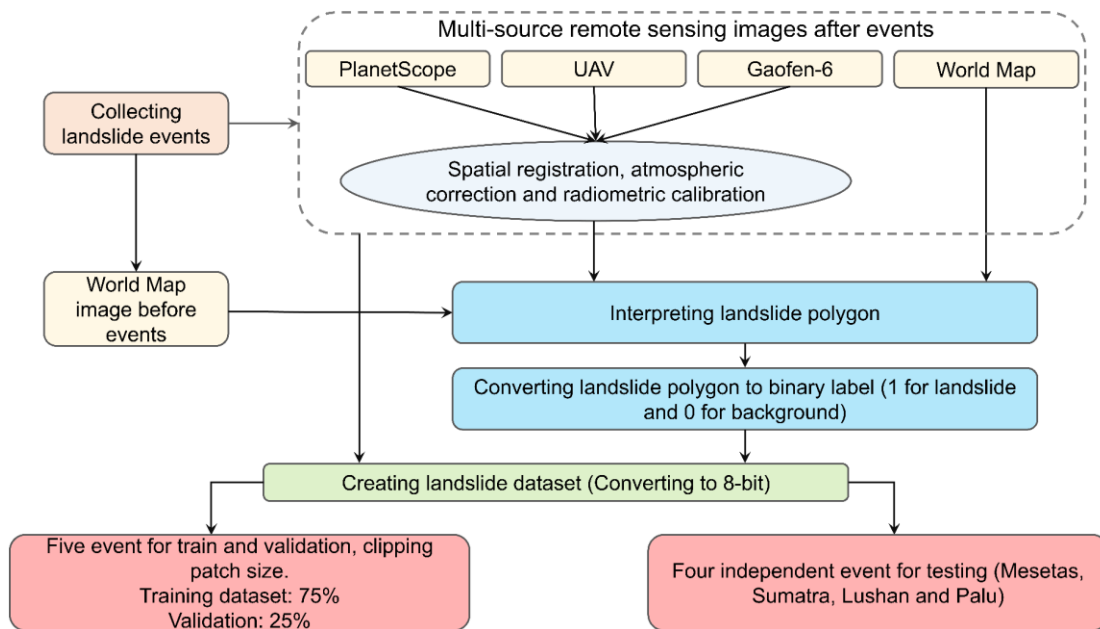
151 In summary, comparing with other remote sensing detection tasks such as land cover/use,  
 152 the currently available landslide datasets are exceedingly scarce, predominantly comprising  
 153 single remote sensing images with low spatial resolutions. Overall, the available landslide  
 154 datasets are exceedingly limited, primarily comprising single remote sensing images with low  
 155 spatial resolution. Most crucially, these datasets lack sufficient annotations of landslide  
 156 instances, exhibit high overlap, and suffer from a dearth of diverse negative samples. As a  
 157 result, they are ill-equipped to tackle the challenges of mapping landslides in large-scale areas  
 158 with complex background objects, especially those sharing spectral and textural characteristics  
 159 with landslide surfaces, such as bare soil and rocks. Furthermore, they fail to provide adequate  
 160 data sources for effectively training large-scale neural network baseline models.

161 **Table.1 Existing landslide dataset statistics**

Dataset	Bands	events	Tiles	Landslides number	Labeling pixels
Bijie landslide	3	1	2773	770	$7.23 \times 10^6$
Landslide4sense	14	4	3799	>30000	$1.76 \times 10^6$
HR-GLDD	4	13	1756	7193	$2.96 \times 10^6$
GVLN	3	17	17	-	$3.24 \times 10^7$
CAS Landslide	3	9	20865	-	$1.95 \times 10^8$

162 3. Globally Distributed Coseismic Landslide Dataset  
163 (GDCLD)

164 The creation of the GDCLD dataset can be broadly divided into two main components:  
165 landslide data collection and remote sensing data processing. In the first part, we compiled  
166 recent landslide events triggered by earthquakes worldwide over the past seven years and  
167 obtained the corresponding remote sensing image. The second part details the process of  
168 annotating landslide labels and the methodology used to create the standard dataset. The  
169 workflow is illustrated in Figure.1.



170

171

**Figure.1** The workflow of producing GDCLD

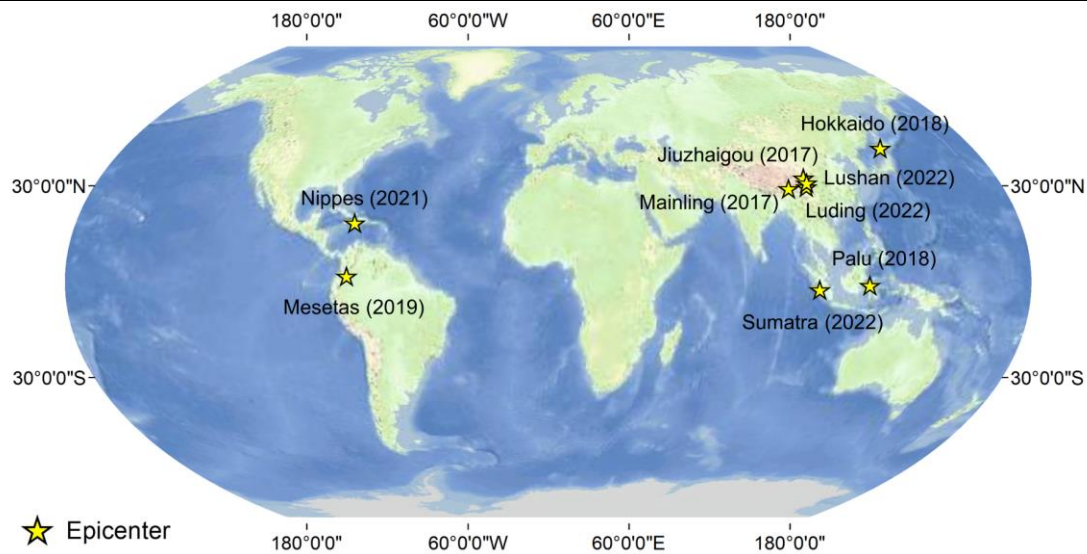
172 3.1 Data collection

173 Our dataset encompasses a catalog of landslides triggered by nine seismic occurrences,  
174 delineated across the Himalayan seismic belt and the Circum-Pacific belt, as depicted in  
175 Figure.2. These regions have witnessed actively seismic events with magnitudes over 5.9,  
176 triggering numerous landslides (Table.2). We obtained data of these locations from various  
177 remote sensing sources. This section delineates the particulars of the seismic events and the  
178 provenance of the remote sensing data.



Table.2 Summary table of landslide event information in GDCLD

Events	Mw	time	Geographic coordinates	Landslide number	Total landslide area (km <sup>2</sup> )
Jiuzhaigou	6.5	2017	(102.82°E, 33.20°N)	2498	14.5
Mainling	6.4	2017	(95.02°E, 29.75°N)	1448	33.6
Hokkaido	6.6	2018	(142.01°E, 42.69°N)	7962	23.8
Palu	7.5	2018	(119.84°E, 0.18°S)	15700	43.0
Mesetas	6.0	2019	(76.19°W, 3.45°N)	804	8.5
Nippes	7.2	2021	(73.45°W, 18.35°N)	4893	45.6
Sumatra	6.1	2022	(100.10°E, 0.22°N)	602	10.6
Lushan	5.9	2022	(102.94°E, 30.37°N)	1063	7.2
Luding	6.8	2022	(102.08°E, 29.59°N)	15163	28.53



★ Epicenter

**Figure.2** Distribution of earthquake-triggered landslide events

### 3.1.1 The 2017 Jiuzhaigou earthquake-triggered landslides

On August 8, 2017, a Mw 6.5 earthquake struck Jiuzhaigou County in Sichuan Province, China (102.82°E, 33.20°N), triggering 2,498 landslides, predominantly shallow surface slides and collapses. The largest landslide covered approximately  $2.3 \times 10^5 \text{m}^2$  (Fan et al., 2018). Jiuzhaigou, situated on the northeastern margin of the Qinghai-Tibet Plateau within the tectonically active zone north of the Longmenshan fault, is part of the Mediterranean Himalayan seismic belt (Fan et al., 2018). The region's average elevation exceeds 3,000m with a maximum

189 relief of 2,228m and a vegetation cover surpassing 70% (Yi et al., 2020; Chen et al., 2019).  
190 Exposed geological formations include various gray-white sandstones and dolomites from the  
191 Devonian, Carboniferous, Permian, Triassic, and Tertiary periods (Fang et al., 2022). Post-  
192 earthquake, we acquired multiple remote sensing images: 0.2m-resolution UAV image (Phase  
193 One IXU1000) on September 22, 2017, 3m-resolution PlanetScope image on October 13, 2017,  
194 and 0.5m-resolution from Map World (Figure.S1).

### 195 **3.1.2 The 2017 Mainling earthquake-triggered landslides**

196 On November 18, 2017, a magnitude 6.4 earthquake struck Mainling County (95.02°E,  
197 29.75°N), resulting in three injuries and affecting 12,000 individuals. The earthquake triggered  
198 over 1,000 landslides, obstructing numerous watercourses and covering a total area of  
199 33.61km<sup>2</sup>, with the largest landslide spanning 4.9km<sup>2</sup> (Hu et al., 2019). Mainling County, located  
200 on the southeastern margin of the Qinghai-Tibet Plateau within the Yarlung Zangbo Grand  
201 Canyon, is part of the Mediterranean Himalayan seismic zone. This region, with altitudes  
202 ranging from 800 to 7,782m and an average elevation of 2,500m, features a maximum elevation  
203 differential of 2,000m and a robust vegetation coverage of 60% (Gao et al., 2023; Chen et al.,  
204 2019). The monsoonal climate here brings annual rainfall between 1,500 and 2,000mm (Huang  
205 et al., 2021). Following the earthquake, we acquired 3m-resolution PlanetScope images on  
206 December 17, 2017, and April 08, 2018, to interpret the landslides (Figure.S2).

### 207 **3.1.3 The 2018 Hokkaido earthquake**

208 On September 6, 2018, a Mw 6.6 earthquake struck Hokkaido, Japan (142.01°E, 42.69°N),  
209 resulting in 44 fatalities and over 660 injuries. Approximately 80% of the casualties were due to  
210 coseismic landslides. The earthquake triggered over 7,800 landslides, causing extensive  
211 damage to infrastructure. The total area affected by landslides was 23.77 km<sup>2</sup>, with the largest  
212 individual landslide covering 0.5km<sup>2</sup> (Wang et al., 2019). The region, which receives an annual  
213 precipitation of 1,200–1,800mm—relatively low compared to other parts of Japan (Yamagishi  
214 and Yamazaki, 2018)—is characterized by sandstone, mudstone, siltstone, and shale  
215 formations, overlain by substantial volcanic sediments (Wang et al., 2019). Following the  
216 **Hokkaido** earthquake, we acquired PlanetScope image with a 3m resolution on December 12,

217 2018, and Map World image with a 0.5m resolution (Figure.S3).

#### 218 **3.1.4 The 2018 Palu earthquake**

219 On September 28, 2018, the Palu region of Sulawesi, Indonesia, was struck by a Mw 7.5  
220 earthquake with a focal depth of 10 km (0.18°S, 119.84°E). A detailed analysis by Shao et al.  
221 (2023) identified approximately 15,700 co-seismic landslides across a 14,600km<sup>2</sup> area, with a  
222 combined landslide area of about 43.0km<sup>2</sup>. These landslides were predominantly concentrated  
223 in the mountainous canyon regions south of the epicenter. This study provides a semantic-level  
224 interpretation of these landslides, which were mainly shallow disruptions (Shao et al., 2023).  
225 However, some larger-scale flow slides, rockfalls, and debris flows were also observed. High-  
226 resolution Map World image (1m) was utilized to support this analysis (Figure.S4).

227 earthquake

#### 228 **3.1.5 The 2019 Mesetas earthquake**

229 The research site is located in the eastern foothills of the Colombian Eastern Cordillera.  
230 On December 24, 2019, the Mesetas Earthquake, with a magnitude of 6.0, struck this region,  
231 as documented by Poveda et al. (2022). The earthquake's epicenter was located at 76.19°W,  
232 3.45°N, triggering approximately 800 co-seismic landslides. The distribution and predominant  
233 orientation of these landslides were influenced by the shear zone confined within the Guapecito  
234 Fault, a subsidiary offshoot of the Algeciras Fault (Poveda et al., 2022). High-resolution  
235 PlanetScope images (3m) was acquired on January 5 and February 12, 2020, to analyze these  
236 phenomena (Figure.S5).

#### 237 **3.1.6 The 2021 Nippes earthquake**

238 On August 14, 2021, a Mw 7.2 earthquake struck the Nippes Mountains in Haiti (73.45°W,  
239 18.35°N). This seismic event, compounded by heavy rainfall from Tropical Storm Grace on  
240 August 16-17, triggered numerous secondary geological hazards across the Tiburon Peninsula.  
241 The disaster resulted in at least 2,246 fatalities and injured over 12,763 individuals (Calais et  
242 al., 2022). The earthquake-induced landslides totaled 4,893, covering an estimated 45.6km<sup>2</sup>,  
243 with the largest individual landslide spanning  $3.1 \times 10^5$  m<sup>2</sup> (Zhao et al., 2022b). The affected area,  
244 with elevations up to 2,300 m (Alpert, 1942), consists mainly of volcanic rocks, such as basalts,

245 and sedimentary formations, particularly limestones (Harp et al., 2016). Post-earthquake, we  
246 utilized 3m-resolution PlanetScope image (August 29, 2022) and 0.5m-resolution Map World  
247 image to assess the damage (Supplementary Figure 6).

248 On August 14, 2021, a seismic event registering Mw 7.2 hit in the Nippes Mountains of  
249 Haiti (73.45°W, 18.35°N). This seismic activity, coupled with substantial rainfall from Tropical  
250 Storm Grace between August 16 and 17, precipitated a significant number of secondary  
251 geological hazards in the Tiburon Peninsula. The calamity resulted in a tragic loss of at least  
252 2,246 lives and inflicted injuries upon more than 12,763 individuals (Calais et al., 2022). The  
253 earthquake triggered a total of 4,893 landslides, covering an estimated area of 45.6km<sup>2</sup>, with  
254 the maximum individual area reaching 3.1×10<sup>5</sup>m<sup>2</sup> (Zhao et al., 2022b). The study area,  
255 characterized by elevations reaching up to 2,300 m above sea level (Alpert, 1942). Comprised  
256 predominantly of volcanic rocks, such as basalts, and sedimentary formations, notably  
257 limestones (Harp et al., 2016). In addition to obtaining 3m-resolution PlanetScope image after  
258 the Nippes earthquake, we also acquired 0.5m-resolution Map World image (Figure.S6).

### 259 **3.1.7 The 2022 Sumatra earthquake**

260 On February 25, 2022, a Mw 6.1 earthquake struck West Sumatra, Indonesia, at a shallow  
261 depth of 4.9 km. The epicenter was located approximately 20 km from Mount Talakmau  
262 (100.10°E, 0.22°N), a compound volcano rising to about 3,000m. Mount Talakmau, active  
263 during the Holocene, consists of andesite and basalt from the Pleistocene-Holocene epoch  
264 (Basofi et al., 2016). The earthquake induced extensive landslides over a 6km<sup>2</sup> area on the  
265 volcano's eastern and northeastern flanks. High-resolution PlanetScope image (3m) from  
266 March 5 and April 24, 2022, captured these landslides (Figure.S7).

### 267 **3.1.8 The 2022 Lushan earthquake**

268 On June 1, 2022, an Mw 5.9 earthquake (102.94°E, 30.37°N) struck Lushan County, China,  
269 resulting in 4 fatalities and 42 injuries, affecting 14,427 individuals. The seismic event triggered  
270 1,063 landslides over a total area of 7.2km<sup>2</sup>, with the largest landslide covering 0.3km<sup>2</sup> (Zhao  
271 et al., 2022a). This region, located on the southeast margin of the Qinghai-Tibet Plateau,  
272 features an average elevation exceeding 2,000m, with altitudes ranging from 557 to 4,115m

273 (Tang et al., 2023). It is characterized by lush vegetation covering 80% of the area and  
274 experiences a subtropical monsoon climate with annual rainfall between 1,100 and 1,300mm  
275 (Chen et al., 2019). The geological composition predominantly consists of exposed sandstones  
276 and mudstones (Zhao et al., 2022a). High-resolution imagery, including 3 m-resolution  
277 PlanetScope images, 0.5m-resolution Map World image, and 0.2m-resolution UAV images  
278 acquired on June 13, 2022, using a Sony ILCE-5100, was collected for the affected region  
279 (Figure.S8).

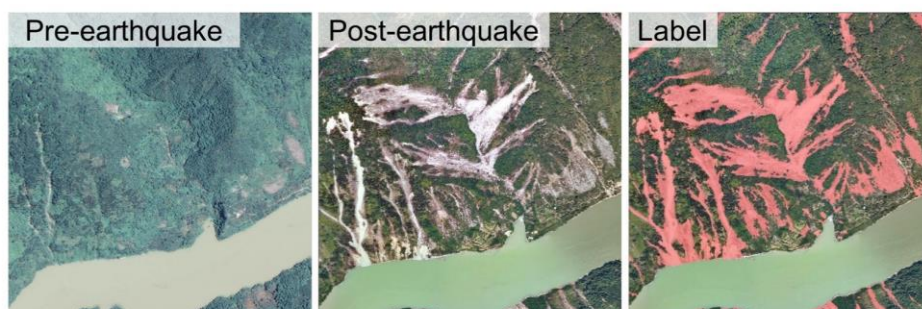
### 280 3.1.9 The 2022 Luding earthquake

281 On September 5, 2022, an Mw 6.8 earthquake struck Luding County, China (102.08°E,  
282 29.59°N), resulting in 93 fatalities. The seismic event triggered approximately 15,000 landslides  
283 over an area of 28.53km<sup>2</sup>, with the largest individual landslide covering 2.4×10<sup>5</sup>m<sup>2</sup> (Dai et al.,  
284 2023). This region lies on the southeastern margin of the Qinghai-Tibet Plateau within the "Y"-  
285 shaped Xianshuihe Fault Zone (Yang et al., 2022b). The geological composition predominantly  
286 includes limestone, sandstone, dolomite, and some intrusive rocks (Dai et al., 2023). In the  
287 aftermath of the earthquake, rapid rescue operations and data collection were undertaken,  
288 utilizing 0.2m-resolution UAV image (acquired on October 7, 2022, via Phase One IXU1000),  
289 3m-PlanetScope image (acquired on September 25, 2022), Map World image (0.5m), and  
290 Gaofen-6 (2m) (Figure.S9).

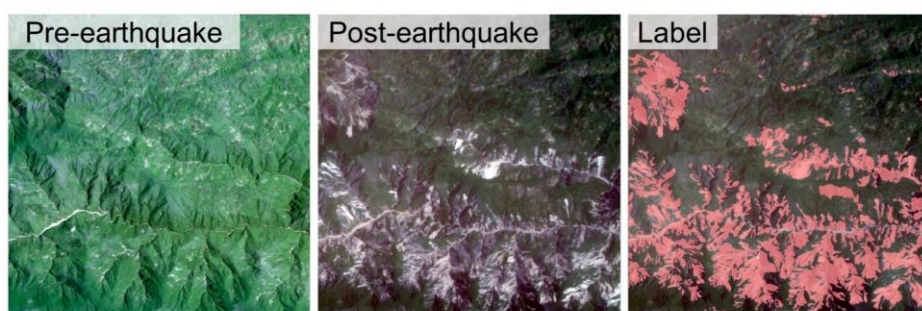
## 291 3.2 Preprocessing of landslide dataset

292 In the aforementioned nine events, the available public data primarily focuses on geological  
293 analysis rather than tasks related to semantic segmentation. After performing multi-source data  
294 spatial registration, atmospheric correction and radiometric calibration on remote sensing  
295 images, we used QGIS for landslide interpretation. These labels were delineated with reference  
296 to pre-earthquake remote sensing imagery and post-earthquake multi-source remote sensing  
297 image. By comparing spectral disparities and analyzing morphological attributes between bi-  
298 temporal images, we mapped the semantic landslide labels. (Figure.3). The mapping of  
299 landslide polygons for these nine events was primarily conducted by a team of five researchers,

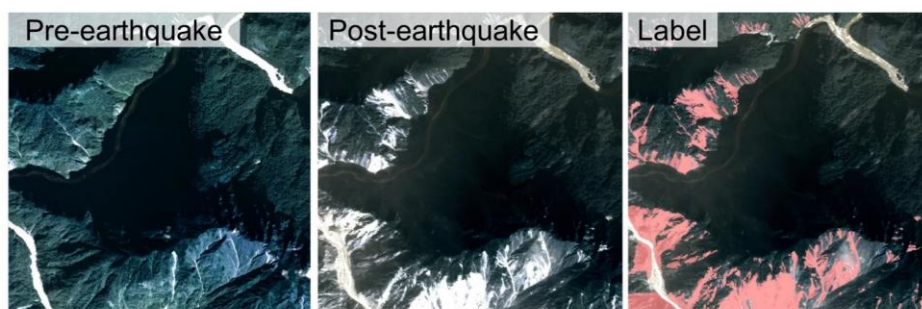
300 including the authors. All team members possess expertise in geology or remote sensing and  
301 were involved in a year-long process of detailed interpretation.



Luding earthquake region (UAV image)



Haiti earthquake region (PlanetScope image)

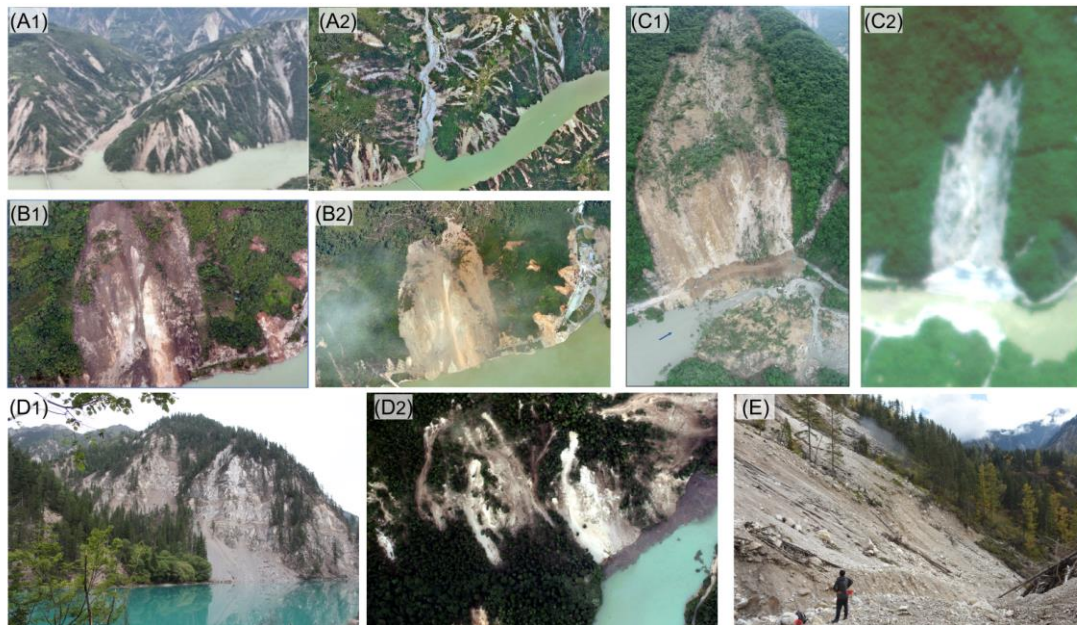


Mainling earthquake region (PlanetScope image)

302  
303 **Figure.3** Remote sensing images before and after the earthquake and landslide interpretation  
304 results (landslides marked in red).

305 Moreover, we actively participated in emergency response and field investigation after  
306 these major earthquakes in China. This further improved the reliability of the landslide  
307 inventories. Figure.4 showcases photographs captured on-site after the Jiuzhaigou earthquake,  
308 Lushan earthquake, and Luding earthquake. Specifically, Figure.4 (A<sub>1</sub>) and 4 (B<sub>1</sub>) were taken  
309 in Luding, Sichuan, depicting the extensive devastation caused by concentrated coseismic  
310 landslides, impacting Wandonghe Village and resulting in severe destruction of local

311 infrastructure. Corresponding aerial photos with a resolution of 0.2m, **Figure.4** (A<sub>2</sub>) and **4** (B<sub>2</sub>),  
 312 offer a comprehensive perspective of the affected area. **Figure.4** (C<sub>1</sub>), taken in Lushan, Sichuan,  
 313 captures the consequences of the earthquake-triggered large landslide dam, which obstructed  
 314 the river channel. The corresponding PlanetScope image, **Figure.4** (C<sub>2</sub>), provides an overhead  
 315 view of the altered landscape. Furthermore, **Figure.4** (D<sub>1</sub>), taken in the Jiuzhaigou Panda Sea,  
 316 illustrates a significant volume of landslide deposits reaching the sea, with the accompanying  
 317 UAV image at a resolution of 0.2m, **Figure.4** (D<sub>2</sub>), offering detailed insights. Lastly, **Figure.4** (E)  
 318 presents a field work photo involved in these surveys. These field investigations serve to  
 319 enhance comprehension and subsequent calibration on our remote sensing interpretation.



320  
 321 **Figure.4** Comparison of field survey photos and remote sensing images: A<sub>1</sub> and A<sub>2</sub> are the  
 322 Wandong landslides induced by the 2022 Luding earthquake; B<sub>1</sub> and B<sub>2</sub> are the Dadu River  
 323 Bridge landslide induced by the 2022 Luding earthquake; C<sub>1</sub> and C<sub>2</sub> are the Baoxing landslides  
 324 induce by the 2022 Lushan earthquake; D<sub>1</sub> and D<sub>2</sub> are the Panda sea landslides induced by  
 325 the 2017 Jiuzhaigou earthquake; E is a photo of field work at Jiuzhaigou.

326 To obtain semantic-level annotations for landslide labels, all remote sensing images were  
 327 converted into RGB images (8-bit). the preprocessing stage was conducted through three steps:  
 328 binary mask generation, data sampling, and image patching. First, utilizing the Rasterio library  
 329 in Python, landslide vector labels for each selected region were transformed into binary masks,

330 where 1 denoted landslide and 0 represented background. Subsequently, regions densely  
 331 populated with landslides were sampled, and both remote sensing images and masks were  
 332 patched and cropped into regular grids, yielding patches of 1,024×1,024 pixels. To mitigate  
 333 interference among patches, overlap parameter was set as 0. Given the obvious imbalance  
 334 between non-landslide and landslide areas, we manually removed most of the images without  
 335 any landslide pixel annotations. The ratios of positive landslide samples and negative non-  
 336 landslide samples were 8.01% and 91.99%, respectively. Table.3 presents detailed information  
 337 regarding different remote sensing data sources for each study case.

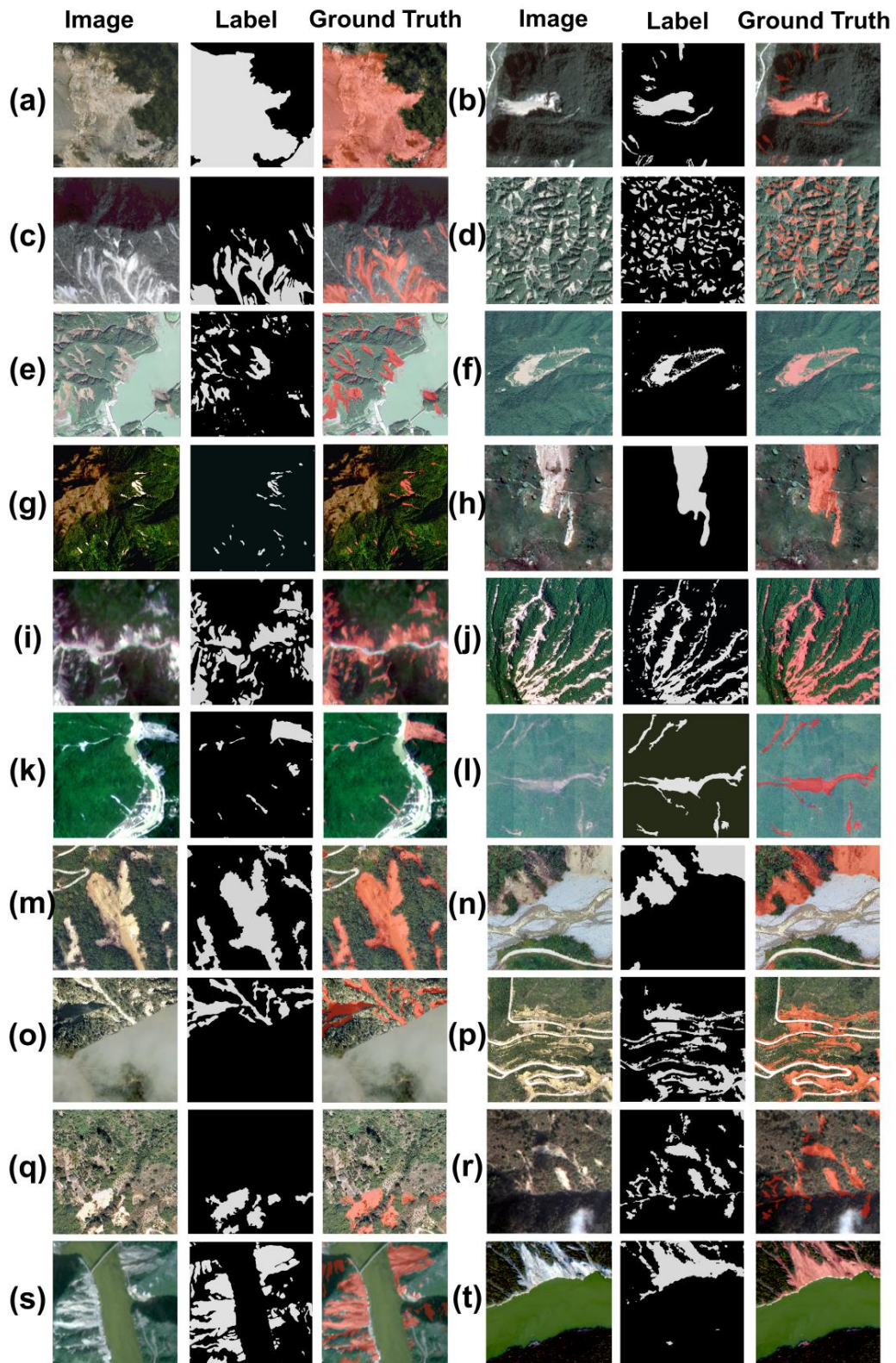
338 **Table.3** Detailed information of each event in GDCLD

Events	Data sources	Resolution	Number of tiles
Jiuzhaigou 2017 (Mw 6.5)	UAV	0.2m	2,288
	PlanetScope	3m	176
Mainling 2017 (Mw 6.4)	PlanetScope	3m	118
Hokkaido 2018 (Mw 6.6)	Map World	0.5m	796
	PlanetScope	3m	123
Palu 2018 (Mw 7.5)	Map World	1m	335
Mesetas 2019 (Mw 6.0)	PlanetScope	3m	144
Haiti 2021 (Mw 7.2)	PlanetScope	3m	238
	Map World	0.5m	404
Sumatra 2022 (Mw 6.1)	PlanetScope	3m	110
Lushan 2022 (Mw 5.9)	UAV	0.2m	210
	Map World	0.5m	182
	PlanetScope	3m	110
Luding 2022	UAV	0.2m	9,252



(Mw 6.6)	Map World	0.5m	1,540
	GF-6	2m	496
	PlanetScope	3m	190
<hr/>			
Sum	-	-	16712
<hr/>			

339        Additionally, to enhance the robustness and generalization capability of deep learning  
340 models, a subset of background noise elements such as clouds, roads, buildings, bare land,  
341 and rocks were manually selected as negative non-landslide samples. The negative samples  
342 can be outlined as follows: diverse roads (Figure.5: (e), (k), (m), (n), (p), (s)), river channels  
343 (Figure.5: (e), (k), (n), (s), (t)), clouds (Figure.5: (o), (r)), barren land (Figure.5: (c), (h), (q)).  
344 Additionally, human-engineered structures and buildings are also considered (Figure.5: (e), (k)).



345

346 **Figure.5** Display of landslide sample data from different study areas and different remote

347 sensing data sources: Jiuzhaigou UAV (a), Jiuzhaigou PlanetScope (b), Mainling PlanetScope

348 (c), Hokkaido PlanetScope(d), Hokkaido Map World (e), Palu Map World (f), Mesetas

349 PlanetScope (g), Haiti Map World (h), Haiti PlanetScope (i), Sumatra PlanetScope (j), Lushan  
350 PlanetScope (k), Lushan UAV (l), Luding UAV(m~q), Luding Map World (r), Luding PlanetScope  
351 (s), and Luding Gaofen-6 (t). The "label" refers to the binary landslide mask, whereas the  
352 "Ground Truth" illustrates the concordance between the annotated and actual landslide in  
353 images.

## 354 4. Experimental setup

355 After the completion of dataset construction, the experimental phase follows. In this section,  
356 we will introduce several semantic segmentation algorithms used for validating the dataset, the  
357 loss functions and accuracy evaluation metrics employed in the experiments, as well as various  
358 hyperparameter settings utilized during the experiments.

### 359 4.1 Segmentation algorithms

360 In this section, we have selected seven of the most popular semantic segmentation  
361 networks, including four models based on the CNN architecture and three based on the  
362 Transformer architecture. These seven algorithms have medium to large-scale parameter sizes  
363 and computational complexities, and show excellent performance in a variety of remote sensing  
364 semantic scenarios, making them suitable for Precision comparison and validation of novel  
365 datasets.

366 (1) UNet: As one of the earliest and most renowned semantic segmentation models, UNet  
367 is distinguished by its unique U-shaped architecture (Ronneberger et al., 2015). This design  
368 facilitates efficient learning and precise localization by combining high-resolution features from  
369 the contracting path with up-sampled outputs from the expanding path. Both the encoder and  
370 decoder in UNet are composed purely of CNN structures (O'shea and Nash, 2015). This  
371 simplicity, along with a relatively small number of parameters, allows UNet to achieve  
372 exceptional accuracy and rapid inference on small datasets. Consequently, it is widely utilized  
373 in applications such as small-scale object classification, change detection, and medical imaging.

374 (2) ResUNet: ResUNet is an advanced variant of the UNet model, incorporating residual

375 connections to enhance its performance and learning efficiency (Diakogiannis et al., 2020). The  
376 key innovation in ResUNet is the integration of residual blocks within both the encoder and  
377 decoder paths, which address the vanishing gradient problem and enable the training of deeper  
378 networks (He et al., 2016). These residual blocks allow the network to learn identity mappings,  
379 facilitating gradient flow through the network and improving convergence rates. Similar to UNet,  
380 ResUNet maintains a U-shaped architecture that combines high-resolution features from the  
381 contracting path with up-sampled outputs from the expanding path, ensuring precise  
382 localization and context capture. The combination of residual connections improves feature  
383 reuse and learning efficiency, enabling ResUNet to effectively improve Recall and small target  
384 detection capabilities in semantic segmentation tasks.

385 (3) DeepLabV3: DeepLabV3, is a semantic segmentation model known for its  
386 sophisticated use of atrous convolution, or dilated convolution (Chen et al. 2018). This  
387 technique allows the network to capture multi-scale contextual information without losing spatial  
388 resolution, addressing the limitations of traditional convolutional networks in dense prediction  
389 tasks. DeepLabV3 incorporates atrous spatial pyramid pooling to robustly segment objects at  
390 multiple scales by applying atrous convolution with different rates in parallel. This model also  
391 integrates features from both the encoder and decoder paths, enhancing the Precision of  
392 boundary delineation. In addition, the architecture of DeepLabV3 utilizes batch normalization  
393 and depth-separable convolution. This design can effectively reduce the complexity and  
394 computational cost of the model, while enabling the model to have stronger feature extraction  
395 capabilities and generalization than simple networks such as UNet.

396 (4) HRNet: High-Resolution Network (HRNet) is noted for its innovative approach to  
397 maintaining high-resolution representations throughout the network (Wang et al., 2020). Unlike  
398 traditional models that gradually down-sample the input to extract features, HRNet preserves  
399 high-resolution features by maintaining parallel high-to-low resolution subnetworks. This design  
400 allows HRNet to integrate multi-scale information effectively, ensuring precise localization and  
401 robust feature representation. The network continuously exchanges information across  
402 different resolutions, resulting in superior accuracy and detailed segmentation results. Due to

403 its ability to retain fine-grained spatial information and adapt to various scales, HRNet excels in  
404 complex tasks such as fine-grained terrain classification, semantic segmentation in urban  
405 scenes, and fine-grained visual detection.

406 (5) UperNet: UperNet employs a pyramid feature extraction method, integrating multi-scale  
407 information to capture contextual details across different resolutions (Xiao et al., 2018; Liu et  
408 al., 2022). It utilizes a Feature Pyramid Network (FPN) backbone for hierarchical feature  
409 extraction, enhanced by a global context integration module to enrich overall scene  
410 understanding. Additionally, UperNet incorporates lateral connections for efficient  
411 communication between feature pyramid levels, ensuring seamless information flow and  
412 accurate segmentation. This sophisticated architecture enables UperNet to achieve superior  
413 segmentation performance, particularly in challenging scenarios with complex scenes and  
414 diverse object scales.

415 (6) SwinUNet: Built upon the Swin Transformer architecture, SwinUNet blends self-  
416 attention mechanisms with UNet for exceptional performance (Cao et al., 2022). It inherits Swin  
417 Transformer's hierarchical feature extraction for capturing both local and global contextual  
418 information efficiently (Liu et al., 2021). The self-attention mechanism enables capturing  
419 nuanced relationships in data. SwinUNet integrates UNet's contracting and expanding paths in  
420 decoding, emphasizing spatial detail preservation. This combination empowers SwinUNet to  
421 excel in tasks requiring precise localization and robust contextual understanding. (7)

422 SegFormer: SegFormer, represents a significant advancement in semantic segmentation by  
423 leveraging a transformer-based architecture (Xie et al., 2021). Unlike traditional CNN  
424 approaches, SegFormer employs a hierarchical transformer encoder to capture multi-scale  
425 contextual information effectively, without relying on complex designs such as positional  
426 encodings or large pre-training datasets. The decoder in SegFormer integrates features from  
427 different scales using lightweight multi-layer perceptron, ensuring efficient and precise  
428 segmentation. This innovative design enables SegFormer to achieve excellent segmentation  
429 results with medium-sized parameters and fast inference speed in high-resolution complex  
430 scenes.

## 431 4.2 Loss function and accuracy evaluation

432 Since the landslide detection is a two-class semantic segmentation task, we choose the  
433 Binary Cross-Entropy (De Boer et al., 2005) as the loss function for model training, whose  
434 mathematical expression is shown as follow:

$$435 \quad L(y, \hat{y}) = -\frac{1}{N} \sum_{i=1}^N [y_i \log(\hat{y}_i) + (1-y_i) \log(1-\hat{y}_i)] \quad (1)$$

436 where  $L$  is the loss function,  $N$  is the number of samples,  $y_i$  is the true label (0 or 1) of the  $i$ -th  
437 sample, and  $\hat{y}_i$  is the predicted probability of the  $i$ -th sample.

438 For accuracy evaluation, the following accuracy indicators are calculated through  
439 confusion matrices (Townsend, 1971): **Precision**, **Recall**, F1 score (Chicco and Jurman, 2020)  
440 and mean intersection over union (mIoU) (Rezatofghi et al., 2019). Their calculation formulas  
441 are as follows:

$$442 \quad \text{Precision} = \frac{TP}{TP+FP} \quad (2)$$

$$443 \quad \text{Recall} = \frac{TP}{TP+FN} \quad (3)$$

$$444 \quad F1 = \frac{2 \times \text{Precision} \times \text{Recall}}{\text{Precision} + \text{Recall}} \quad (4)$$

$$445 \quad \text{mIoU} = \frac{1}{N} \sum_{i=1}^N \frac{TP_i}{TP_i + FP_i + FN_i} \quad (5)$$

446 where the TP is the True Positive, FP is the False Positive, TN is the True Negative and FN is  
447 the False Negative.

## 448 4.3 Equipment and Parameter

449 The deep learning framework employed in this study is conducted based on PaddlePaddle  
450 2.3.2 (Ma et al., 2019), with the environment configured for Python 3.8, CUDA 11.2, and CuDNN  
451 8.3.0. The experimental setup encompasses Intel Xeon CPU, W2255, 3.7GHz, equipped with  
452 256GB of system memory. The GPU infrastructure consists of Tesla V100, with 32GB of video  
453 memory. The operating system employed is Ubuntu 20.04. The model's optimizer is selected  
454 as AdamW (Loshchilov and Hutter, 2017), with an initial learning rate of 0.0006, beta1 set to  
455 0.9, beta2 to 0.999, weight decay to 0.01 and epoch to 100.

## 456 5. Results

457 To validate the accuracy of the GDCLD dataset, this study selected four types of remote  
458 sensing images (UAV, PlanetScope, Map World image, and Gaofen-6) from five seismic events  
459 (Luding, Jiuzhaigou, Hokkaido, Mainling, and Nippes) as training and validation datasets for  
460 model construction and accuracy evaluation. The ratio of training dataset to validation dataset  
461 is 3:1. To further assess the generalization ability of this dataset, we chose three types of remote  
462 sensing images (UAV, PlanetScope, and Map World image) from four independent seismic  
463 events (Lushan, Mestas, Sumatra, and Palu) as the test dataset. Considering the geographical  
464 distribution, these four regions, located on different continents and characterized by distinct  
465 tectonic settings and climatic conditions, ensure complete independence from the training  
466 dataset. From the perspective of data sources, the four study areas represent three major types  
467 of remote sensing imagery: PlanetScope, UAV, and Map World. Additionally, the UAV sensor  
468 used in the Lushan area is different from those used in other regions. This data partitioning  
469 strategy is designed to rigorously evaluate the generalization capability of the GDCLD-trained  
470 model.

471 We conducted evaluations on our dataset utilizing the aforementioned seven semantic  
472 segmentation algorithms. After each model is trained for 100 epochs, we meticulously  
473 examined the performance of the GDCLD dataset in landslide identification. we present the  
474 performance of the seven algorithms on the validation dataset in Table.4.

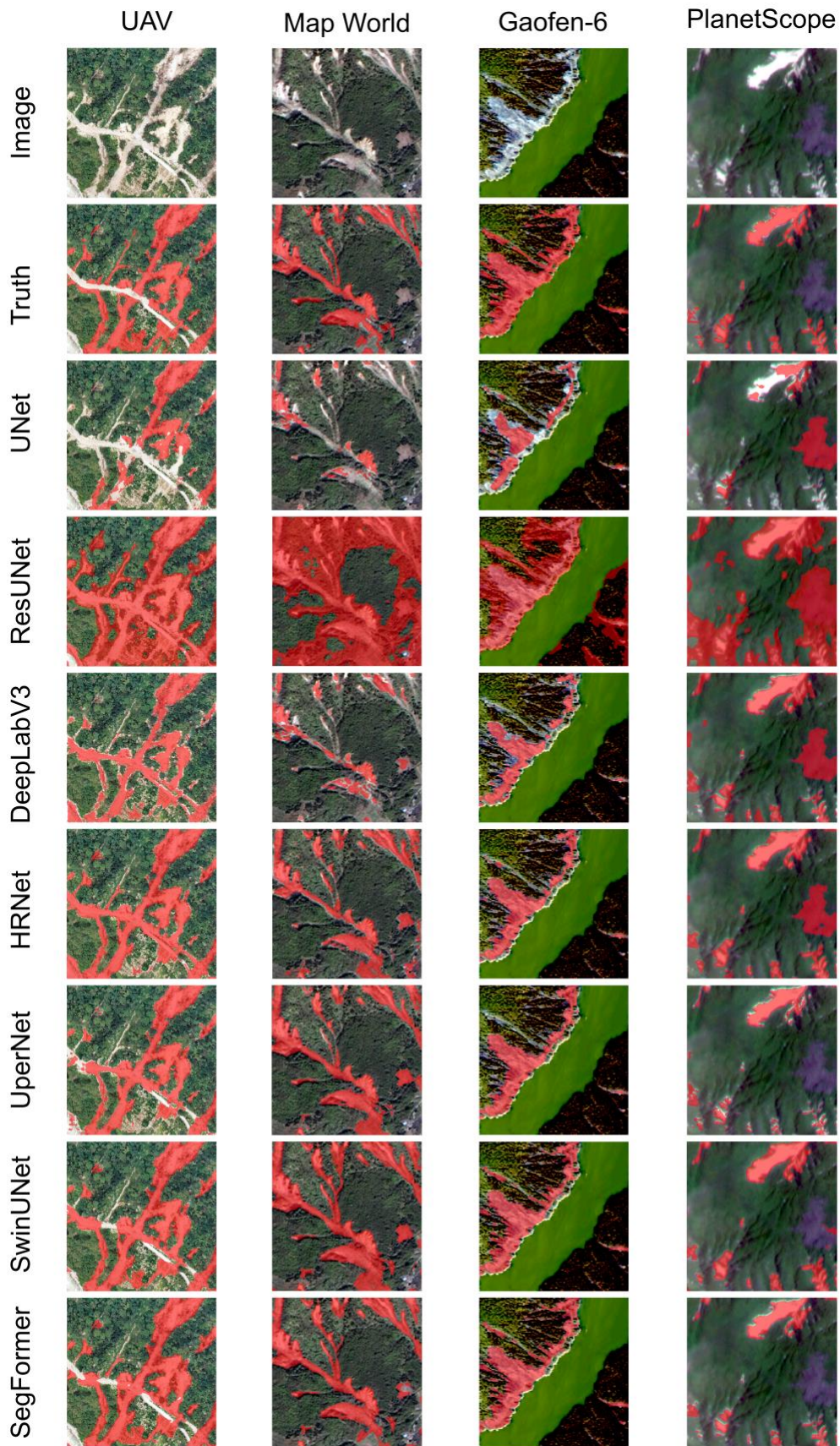
475 Among these seven algorithms, UNet, ResUNet, DeepLabV3, and HRNet serve as neural  
476 network models with convolutional structures, whereas UperNet, SwinUNet, and SegFormer  
477 are based on transformer-based neural network architectures. From Table.4, it is evident that  
478 Transformer-based semantic segmentation models exhibit superior performance compared to  
479 models based on convolutional structures. Overall, the mIoU of the seven algorithms on  
480 GDCLD validation set spans from 71.07% to 85.06%. Notably, UNet demonstrates the least  
481 detection with the mIoU and F1 score of 71.07% and 79.54%. In contrast, SegFormer yields  
482 the best performance with the accuracy of 91.35%, Recall of 91.70%, F1 score of 91.52%, and

483 mIoU of 85.06%. Figure.6 illustrates the detection results of different models across various  
484 remote sensing data sources. it can be seen that transformer-based semantic segmentation  
485 models achieve superior segmentation outcomes.

486 **Table.4** Comparison of result on GDCLD validation dataset

Method	Backbone	Precision (%)	Recall (%)	F1 (%)	mIoU (%)
UNet	-	77.05	82.01	79.54	71.07
ResUNet	ResNet-50	78.17	86.48	82.11	71.94
DeepLabV3	ResNet-50	81.27	86.96	84.02	74.61
HRNet	HRNet-48	81.88	87.21	84.46	75.19
UperNet	ViT-B16	88.18	90.64	89.39	81.97
SwinUNet	-	89.78	<b>92.01</b>	90.72	83.68
SegFormer	MiT-B4	<b>91.35</b>	91.70	<b>91.52</b>	<b>85.06</b>





487

488

**Figure.6** Comparative results of different algorithms on validation dataset

489 To demonstrate the robustness and generalization capability of the dataset-trained models  
490 in other environment, we conducted testing by using four independent events, as illustrated in  
491 Table.5. Overall, the mIoU performance of the algorithms trained on GDCLD ranges from 56.09%  
492 to 72.84%. SegFormer exhibits the best performance, achieving Precision of 77.09%, Recall of  
493 87.09%, F1 score of 81.88%, and mIoU of 72.84%. we present detailed results of six types of  
494 remote sensing images in these four events in Table.6. The overall mIoU ranges from 69.01%  
495 to 82.31%, while the F1 ranges from 80.63% to 89.30%. Furthermore, we noticed a remarkable  
496 imbalance between Recall and Precision in the predicted results. The Recall is always higher  
497 than the Precision, as it is crucial to not miss any important landslides for disaster assessment  
498 and rescue operations. From the perspective of remote sensing sensors, except for the  
499 Sumatra incident, higher resolution was directly related to better landslide detection  
500 performance.

501 **Table.5** Comparison of result on test dataset

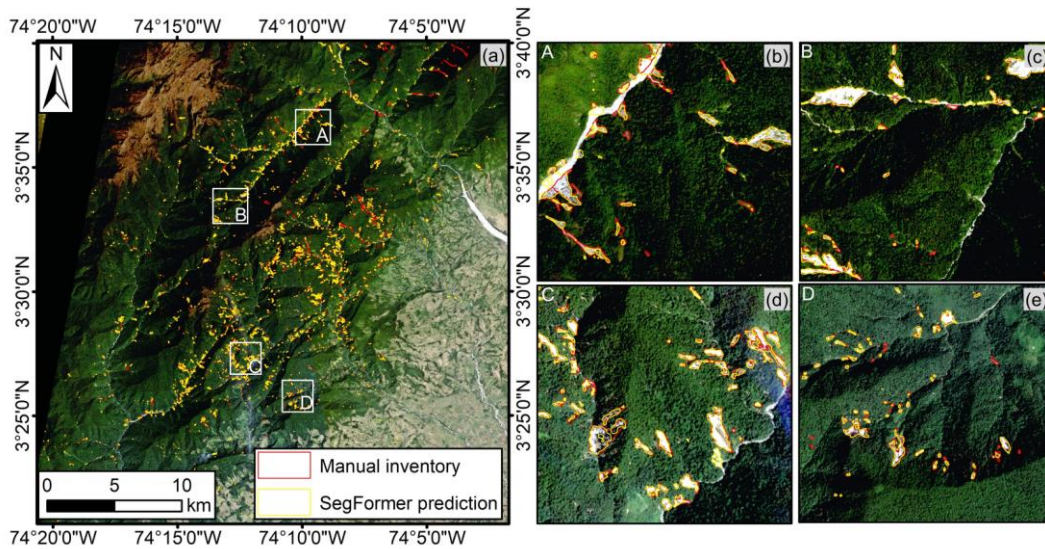
Method	Backbone	Precision (%)	Recall (%)	F1 (%)	mIoU (%)
UNet	-	61.69	61.22	61.45	56.09
ResUNet	ResNet-50	66.56	64.46	65.49	57.06
DeepLabV3	ResNet-50	65.26	67.75	66.48	59.73
HRNet	HRNet-48	65.52	72.03	68.62	61.79
UperNet	ViT-B16	69.96	78.08	73.80	65.42
SwinUNet	-	71.56	82.26	76.54	67.18
SegFormer	MiT-B4	<b>77.09</b>	<b>87.09</b>	<b>81.88</b>	<b>72.84</b>

502 **Table.6** Detection results of SegFormer in different events

Events	Image type	Precision (%)	Recall (%)	F1 (%)	mIoU (%)
	UAV	74.72	90.35	81.80	72.96
Lushan	Map World	76.18	87.35	81.38	71.92
	PlanetScope	81.50	82.28	81.78	69.05
Palu	Map World	73.48	91.24	81.40	71.12
Mesetas	PlanetScope	80.26	80.97	80.63	69.01
Sumatra	PlanetScope	83.57	97.45	89.30	82.31

503 Figures.7 to 10 respectively illustrate the detection results for Mesetas (PlanetScope),

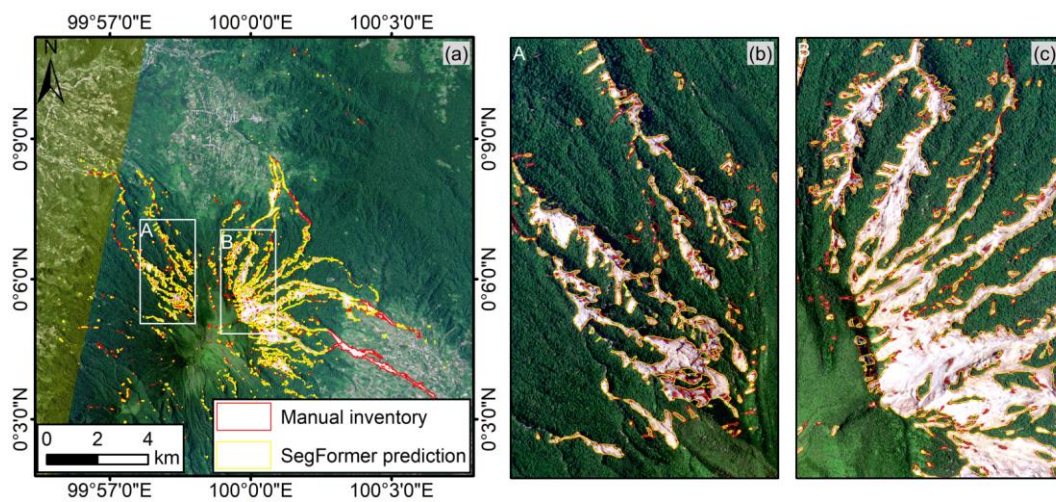
504 Sumatra (PlanetScope), Palu (Map World image), and Lushan (UAV). The F1 score of the  
505 Mesetas event model is 80.63%, with **Recall and Precision** exhibiting relative balance. As  
506 observed in Figure.7, our model demonstrates strong capabilities in detecting and segmenting  
507 the majority of landslides, particularly in regions of mountainous slopes (Figure.7 (d)). In areas  
508 affected by mountain shadows (Figure.7 (b, c, e)), as expected, since, pixel signatures of  
509 shadows are very different than those of landslides. The model effectively identifies most large  
510 landslides but exhibits some omissions in detecting small landslides. In the Sumatra event, we  
511 attained remarkably excellent detection results, with F1 score of 89.30%, Recall of 97.45%, and  
512 Precision of 83.57%, Recall is 13.88% higher than Precision. As illustrated in Figure.8, the  
513 model effectively identifies nearly all landslides (Figure.8 (b, c)). However, there are instances  
514 of missed landslide detection in the lower-right corner of Figure.8 (a). This is due to the apparent  
515 confusion between the landslide accumulation area and river channels, resulting in sub-optimal  
516 detection. In the Palu event, our F1 score yielded a result of 81.40%, with Recall reaching 91.24%  
517 and Precision by 73.48%, Recall is 17.76% higher than Precision. As depicted in Figure.9, the  
518 detection outcomes effectively discriminate between numerous cloud obscuration, bare lands,  
519 and buildings, underscoring the positive efficacy of augmenting negative samples in our dataset  
520 to improve the model's detection capabilities. Similarly, for the Lushan event captured by UAV,  
521 we achieved the F1 score of 81.80%, with Recall and Precision of 90.35% and 74.72%, Recall  
522 exceeding Precision by 15.63%. As shown in Figure.10, in the UAV data, the model  
523 demonstrates exceptional segmentation capabilities for large-scale landslides (Figure.10 (b, c,  
524 d)), while its detection performance for some small-scale disasters is less satisfactory. Overall,  
525 the model trained based on GDCLD demonstrated excellent generalization capabilities across  
526 four independent test datasets. It successfully detected all major landslides and effectively  
527 segmented landslide boundaries. More importantly, the model effectively excluded background  
528 noise from river channels, bare ground in residential areas, and cloud region, showcasing its  
529 remarkable robustness.



530

531 **Figure.7** Mesetas PlanetScope dataset. (a) Regional aerial view. (b-e) Detection results of four

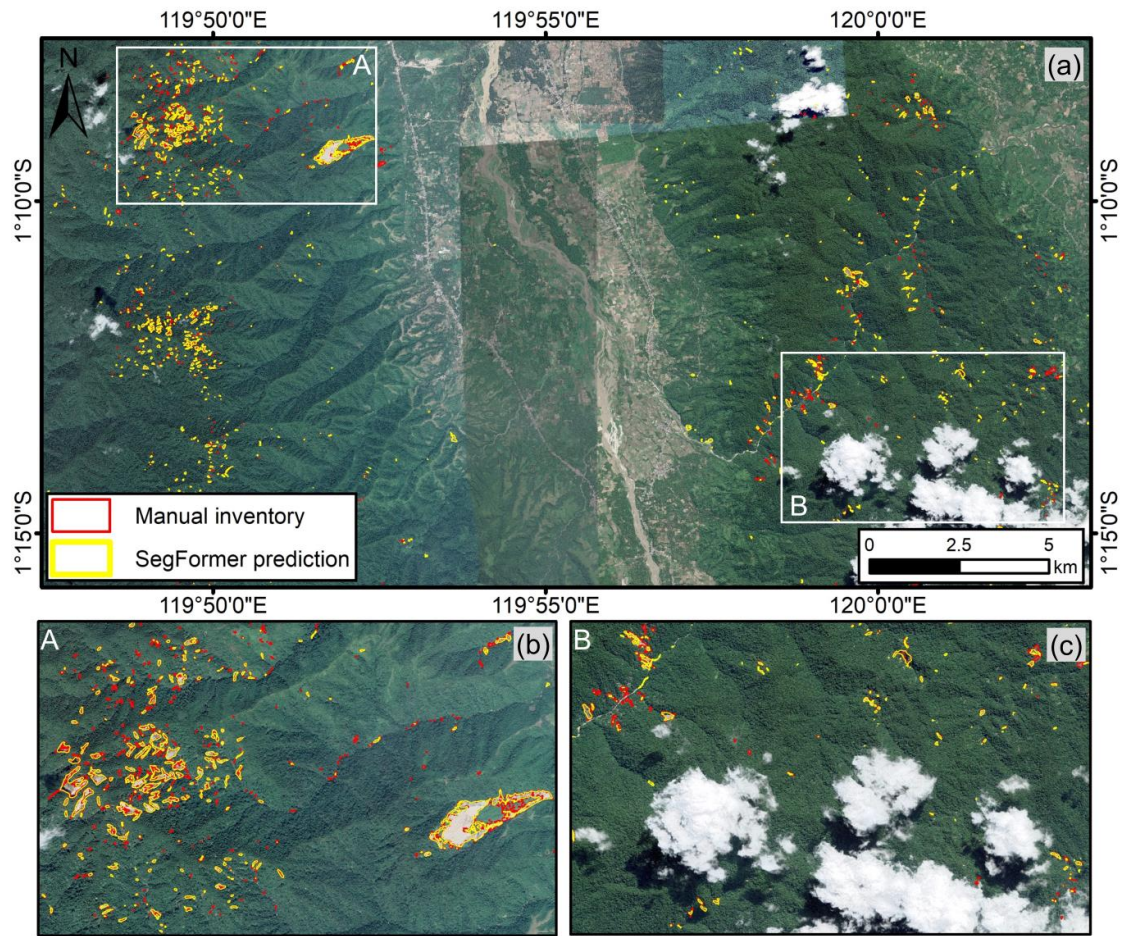
532 magnified areas.



533

534 **Figure.8** Sumatra PlanetScope dataset. (a) Regional aerial view. (b-c) Detection results of two

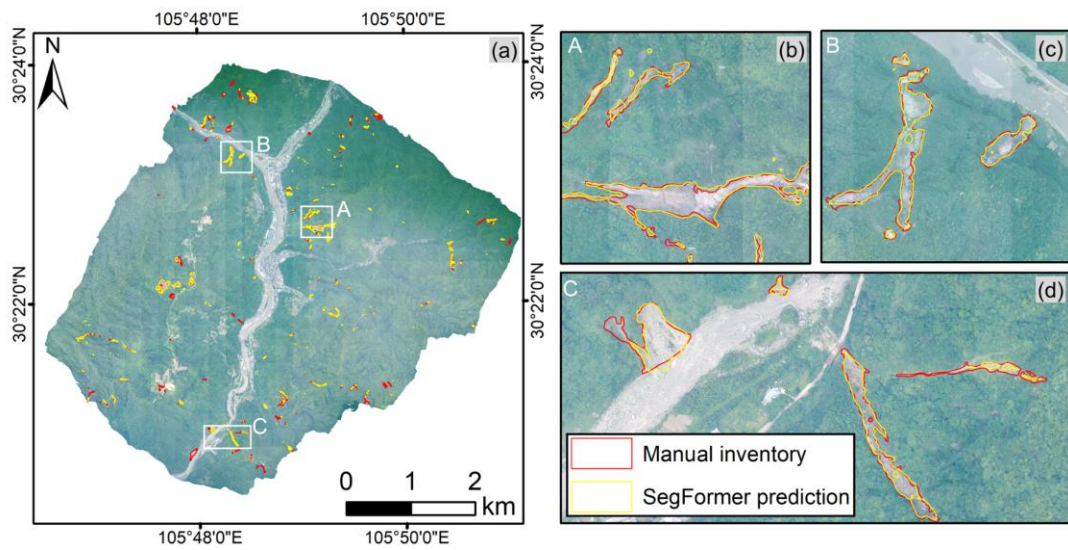
535 magnified areas.



536

537 **Figure.9** Palu Map World dataset. (a) Regional aerial view. (b-c) Detection results of two  
 538 magnified areas.

539



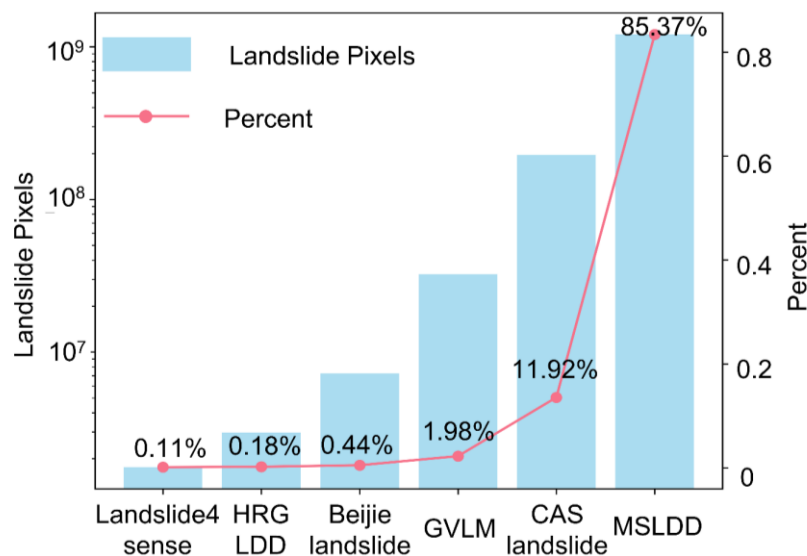
540

541 **Figure.10** Lushan UAV dataset. (a) Regional aerial view. (b-d) Detection results of three  
 542 magnified areas.

## 543 6. Discussion

### 544 6.1 Sample richness of GDCLD

545 The GDCLD dataset stands out as the most extensive and comprehensive repository of  
546 landslide data currently available, encompassing landslide data from various geographic  
547 environments and multiple remote sensing sources. the annotated landslide labels within this  
548 dataset tally up to approximately  $1.39 \times 10^9$  pixels, roughly six times as many annotations as all  
549 the other publicly accessible landslide datasets (Figure.11). Additionally, this dataset includes  
550 a variety of negative samples with optical characteristics similar to landslides which can  
551 significantly enhance the model's generalization capability. In contrast to other datasets, which  
552 are limited to training small-scale semantic segmentation models like UNet and DeepLabV3  
553 (Xu et al., 2024; Meena et al., 2022; Ghorbanzadeh et al., 2022), the GDCLD dataset can  
554 effectively train large-scale semantic segmentation models such as Transformers. Moreover,  
555 unlike Sentinel-2 and Landsat satellite image, where moderate spatial resolutions can limit the  
556 accurate delineation of landslide boundaries, GDCLD provides remarkably high spatial  
557 resolutions (0.2m~3m) and diverse spectral characteristics. This dataset not only performs well  
558 in landslide mapping across diverse geographical settings, but also serves as a baseline  
559 dataset for transfer learning in landslide detection.



560

561

**Figure.11** Statistical comparison of landslide pixels in different landslide datasets.

## 562 6.2 Enhancement in model generalization

563 In the GDCLD dataset, a general selection of remote sensing data from multiple sources  
564 enhances the overall generalization capability of the landslide identification model. To  
565 substantiate this assertion, we conduct a comparative analysis between models trained by  
566 single- and multi-source datasets. The datasets from different sensors are segregated, and the  
567 SegFormer, which is an advanced and widely used transformer-based algorithm, is applied to  
568 train the landslide models. Their performance was verified by their respective test dataset as  
569 well as an independent event of Lushan earthquake.

570 The accuracy metrics for the validation dataset are presented in Table.7. Across four  
571 remote sensing sources—PlanetScope, Gaofen-6, Map World, and UAV—models trained on  
572 single-source datasets consistently demonstrate higher performance on test samples, with  
573 mIoU indices surpassing those of multi-source datasets by 2.26%, 1.63%, 0.64%, and 0.13%,  
574 respectively. However, a noteworthy observation emerges when models are transferred to the  
575 independent Lushan earthquake case (Table.8). The model trained on the multi-source dataset  
576 achieves significantly enhanced performance compared to the model derived from single-  
577 source counterpart. The mIoU of UAV-, Map World- and PlanetScope based datasets are  
578 improved by 8.16%, 7.95% and 0.09%. As depicted in Figure.12, the models trained by multi-  
579 source images exhibit higher recalls, accurate landslide boundaries, and robust resistance to  
580 interference. The yellow circle highlights the enhancements of models trained by multi-source  
581 images compared to single-source images. From the perspective of data sources, Map World  
582 contains different types of images (such as Gaofen and Jilin), encompassing multitude of  
583 spectral responses across these sensors. the UAV image in the Lushan event utilize the sensor  
584 different from those in the Luding and Jiuzhaigou event, resulting in noticeable spectrum  
585 differences in images. Consequently, compared to a single remote sensing source, the  
586 generalization capability of the models trained by multi-source images demonstrate a more  
587 pronounced improvement. In contrast, the PlanetScope image, obtaining from the same  
588 satellite sensors, exhibits smaller spectral variations in various images. As a result, the model  
589 trained on both single and multi-source datasets achieve similar performance. This highlights

590 the importance of datasets with diverse images sources for enhanced model performance in  
 591 landslide mapping. This indicate that the utilization of multi-source remote sensing datasets  
 592 enables the model to learn the spectral characteristics of the images from diverse sensors.  
 593 Hence, the model trained by GDCLD possesses enhanced generalization ability and  
 594 robustness, enabling it to effectively perform landslide mapping in independent cases without  
 595 prior knowledge.

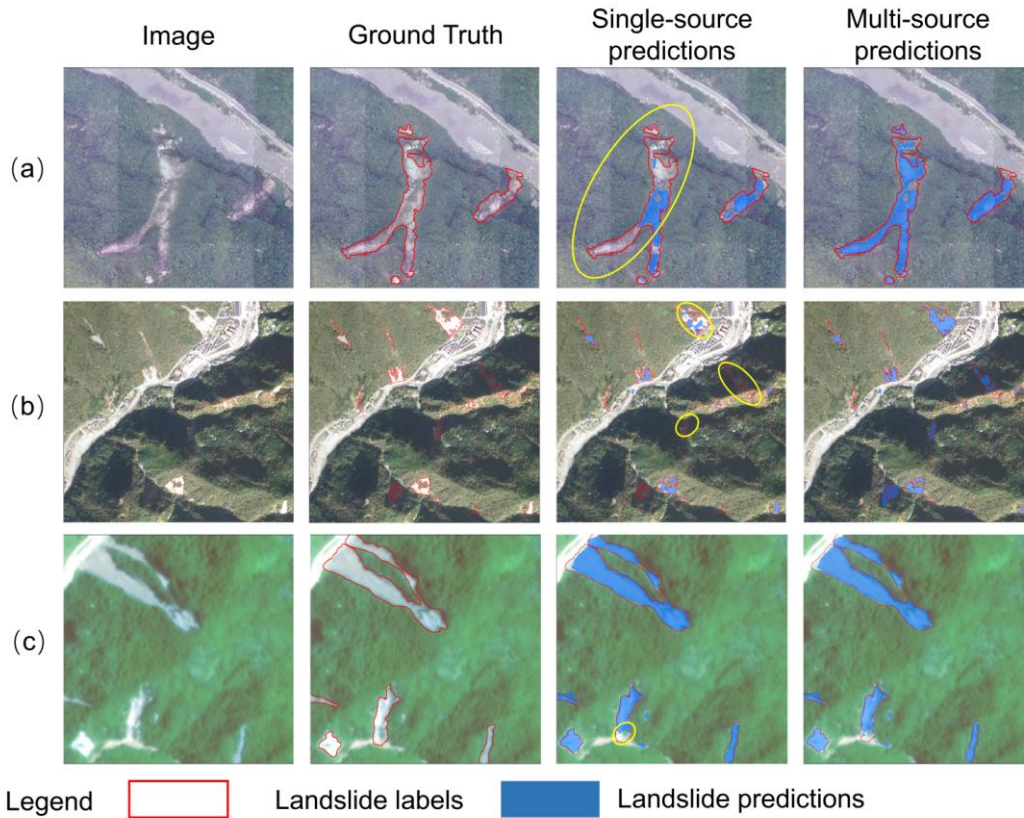
596 **Table.7** GDCLD performances on validation dataset through single- and multi-source dataset

Data source	Data type	Precision (%)	Recall (%)	F1 (%)	mIoU (%)
Single source	UAV	<b>92.20</b>	<b>92.90</b>	<b>92.54</b>	<b>87.07</b>
	PlanetScope	<b>87.98</b>	<b>87.81</b>	<b>87.89</b>	<b>80.11</b>
	Map World	<b>86.49</b>	<b>90.01</b>	<b>88.21</b>	<b>80.66</b>
	Gaofen-6	<b>91.25</b>	<b>88.04</b>	<b>89.62</b>	<b>83.61</b>
Multiple source	UAV	91.91	92.64	92.27	86.94
	PlanetScope	85.01	87.79	86.37	77.85
	Map World	86.42	89.12	87.74	80.02
	Gaofen-6	90.49	85.20	87.77	81.98

597 **Table.8** GDCLD performances on unseen dataset through single- and multi-source dataset

Data source	Data type	Precision (%)	Recall (%)	F1 (%)	mIoU (%)
Single source	UAV	64.92	<b>90.68</b>	75.67	64.80
	PlanetScope	81.25	<b>82.29</b>	81.75	68.96
	Map World	68.39	80.16	73.81	63.97
Multiple source	UAV	<b>74.72</b>	90.35	<b>81.80</b>	<b>72.96</b>
	PlanetScope	<b>81.50</b>	82.28	<b>81.78</b>	<b>69.05</b>
	Map World	<b>76.18</b>	<b>87.35</b>	<b>81.38</b>	<b>71.92</b>





598

599 **Figure.12** Comparative results of ablation experiments between multi- and single-source (a).  
600 UAV, (b). Map World, (c). PlanetScope

### 601 6.3 Comparison with existing landslide datasets and models

602 To assess the robustness and generalization capabilities of the GDCLD dataset, we  
603 employ SegFormer trained on the GDCLD dataset (**GDCLD-S model**) to identify landslides  
604 within three distinct datasets: HR-GLDD, GVLM, and CAS. Initially, we standardize the data  
605 from these three datasets into 1024×1024 remote sensing tiles. Subsequently, utilizing the  
606 **GDCLD-S model**, we conduct landslide identification across all these datasets. Table.9  
607 demonstrates favorable performance of the model across these diverse datasets. For instance,  
608 in the HR-GLDD dataset, which shares similarities with the PlanetScope image in GDCLD, the  
609 model achieves an mIoU of 76.97%, indicating a balance between Precision and Recall metrics.  
610 Similarly, when applied to the GVLM dataset, leveraging Map World image, our dataset exhibits  
611 robust predictive outcomes, resulting in a comprehensive mIoU of 70.07%. Likewise, for the  
612 CAS dataset, GDCLD demonstrates strong generalization capabilities, yielding an outstanding

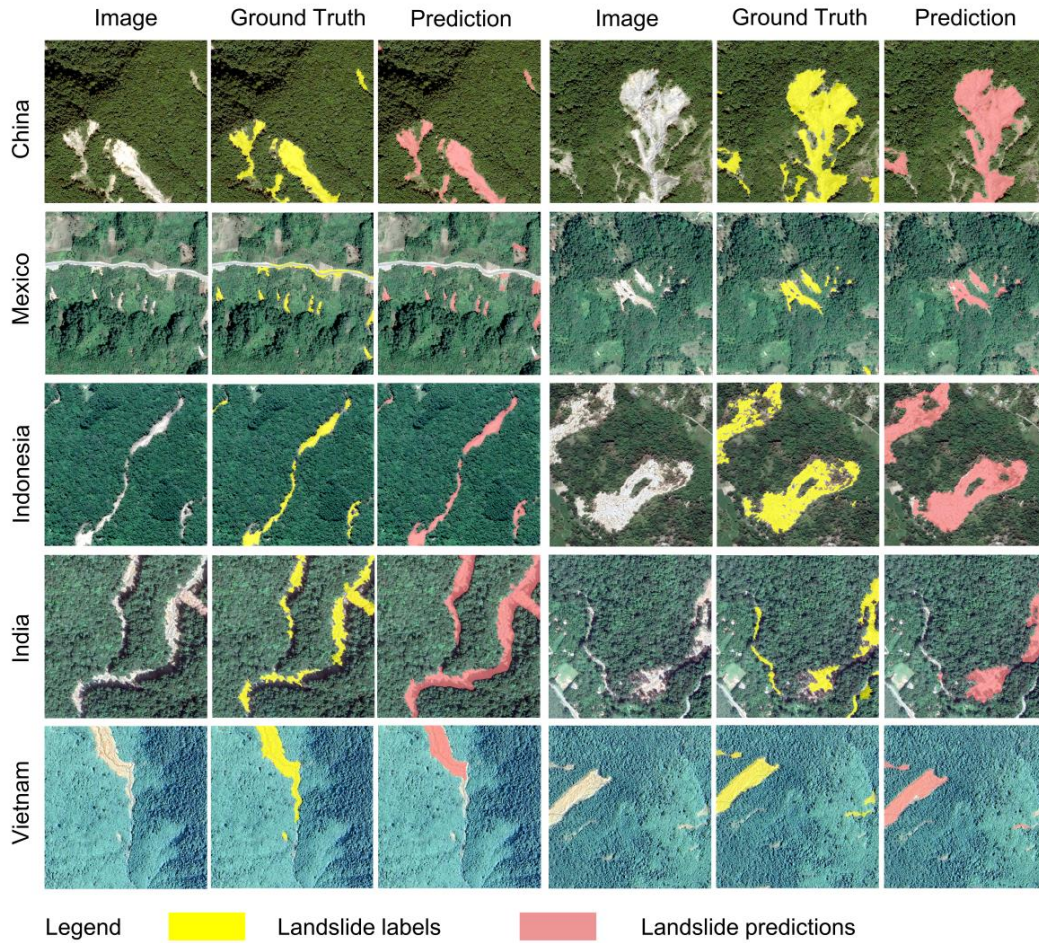
613 comprehensive metric with mIoU = 76.91%, alongside balanced Recall and Precision metrics.

614 Although all landslide samples contained in GDCLD are induced by seismic activity, our  
615 model demonstrates good detection capabilities for rainfall-induced landslides. These two  
616 categories exhibit distinct spectral characteristics from their surrounding environments.  
617 Consequently, models trained on GDCLD exhibit proficient detection capabilities for rainfall-  
618 induced landslides. We present the identification performance of GDCLD-based model for  
619 rainfall-induced landslides from the GVLM dataset in [Table.9](#) and [Figure.13](#). [Figure.13](#)  
620 underscores the excellent detection performance of the GDCLD-S model on rainfall-induced  
621 landslides in the GVLM dataset. Despite occasional misclassifications of small-size targets, the  
622 model effectively delineates the majority of rain-induced landslides. the [Precision](#) metrics in  
623 [Table.8](#) affirm this observation with an mIoU reaching 78.22% and both [Recall](#) and [Precision](#)  
624 exceeding 85%. This highlights the robust generalization capability of the model trained by our  
625 dataset, enabling effective identification of rainfall-induced landslides.

626

**Table.9** Validation results of other public datasets

Dataset	Precision (%)	Recall (%)	F1 (%)	mIoU (%)
HR-GLDD	84.88	86.81	85.84	76.97
GVLM	72.83	87.54	80.68	70.07
CAS	82.95	86.35	84.62	76.91
GVLM-rainfall	85.88	86.71	86.29	78.22



628 **Figure.13** Detection results of rainfall landslides by GDCLD-S model. Map credits: GVLM.

629         In addition to the aforementioned analyses, we compare the performance of GDCLD with  
630 other two datasets, GVLM and CAS. Specifically, we train landslide detection models using the  
631 SegFormer algorithm on the GVLM and CAS datasets, denoted as GVLM-S and CAS-S,  
632 respectively, with identical training parameters as previously described. Furthermore, we also  
633 use the DeepLabV3 to train the CAS-D model based on the CAS dataset and use it for  
634 comparison of landslide detection (Xu et al., 2024). Subsequently, the GDCLD-S, CAS-S, CAS-  
635 D and GVLM-S models were applied to identify landslides in the Lushan area using three  
636 distinct remote sensing data sources: UAV, PlanetScope, and Map World. The results of this  
637 comparison are presented in Table 10. From Table 10, it is evident that the GDCLD-S model  
638 outperformed CAS-S, CAS-D and GVLM-S across all three remote sensing datasets, achieving  
639 mIoU of 72.96%, 69.05%, and 71.92% on UAV, PlanetScope, and Map World. In contrast, CAS-  
640 S records mIoU values of 62.03%, 56.86%, and 60.35% for the same datasets, respectively,

641 which is better than the CAS-D model trained with DeepLabV3, and also illustrates the  
 642 advantages of the transformer architecture over the CNN architecture. Notably, GDCLD-S  
 643 exhibited a significantly higher Recall than the other two models and also demonstrated an  
 644 advantage in Precision. Overall, GDCLD-S, along with CAS-S, exhibited superior performance  
 645 compared to the single-source data model GVLM-S, particularly in handling multisource remote  
 646 sensing images. The extensive landslide data and negative samples included in GDCLD-S  
 647 further contributed to its enhanced robustness against noise and improved Recall in landslide  
 648 detection.

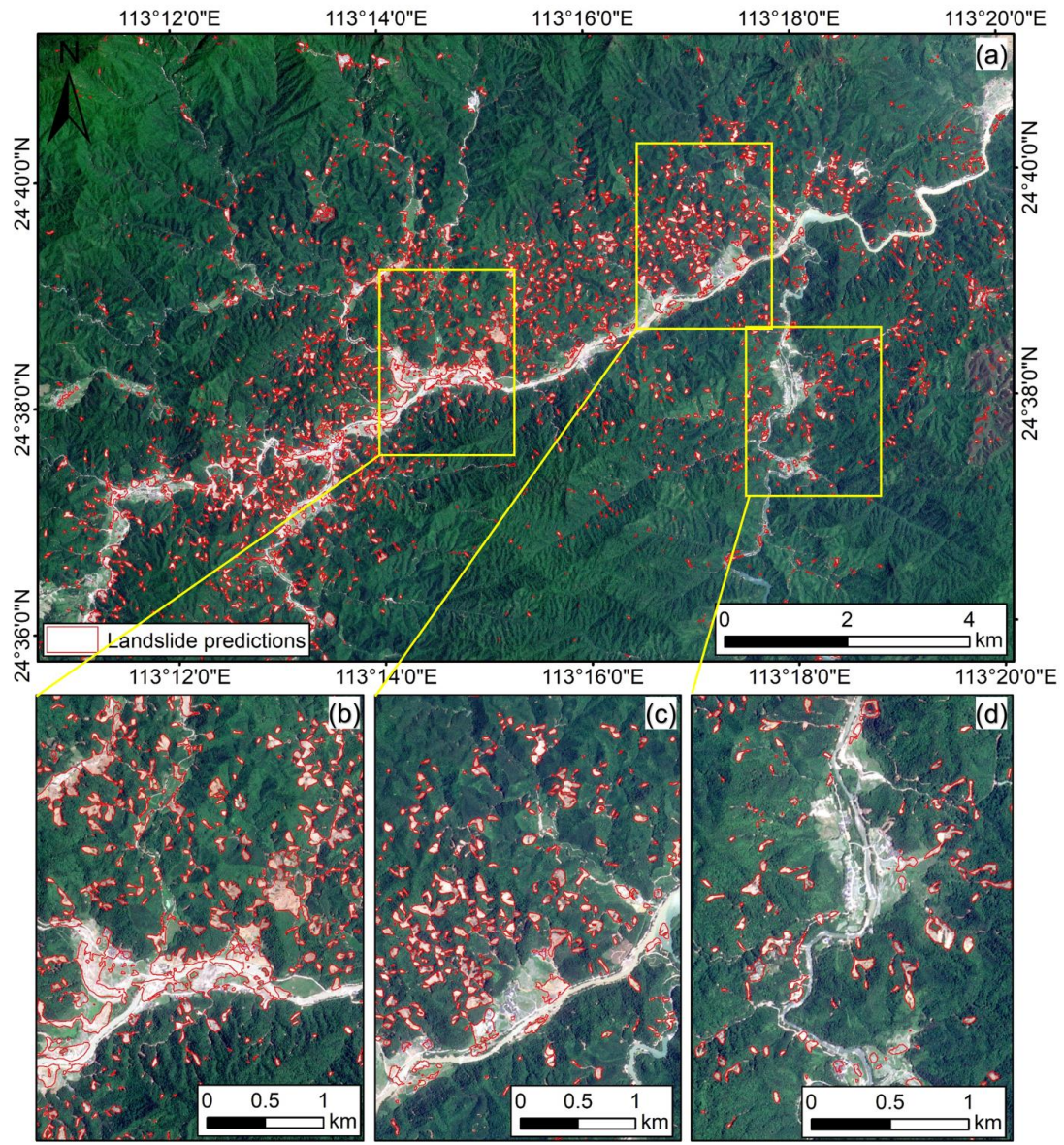
649 **Table.10** Performance comparison of GDCLD-S, GVLM-S, CAS-S, CAS-D on the Lushan  
 650 dataset

Model	Data type	Precision (%)	Recall (%)	F1 (%)	mIoU (%)
CAS-D	UAV	72.73	55.34	62.88	57.91
	PlanetScope	52.07	56.05	53.93	52.86
	Map World	61.79	70.50	64.9	58.11
GVLM-S	UAV	73.03	54.84	57.67	53.41
	PlanetScope	60.13	53.40	54.82	51.52
	Map World	<b>77.71</b>	66.40	71.56	63.97
CAS-S	UAV	74.08	67.05	69.95	62.03
	PlanetScope	58.56	76.57	66.40	56.86
	Map World	75.02	64.65	68.37	60.35
GDCLD-S	UAV	<b>74.72</b>	<b>90.35</b>	<b>81.80</b>	<b>72.96</b>
	PlanetScope	<b>81.50</b>	<b>82.28</b>	<b>81.78</b>	<b>69.05</b>

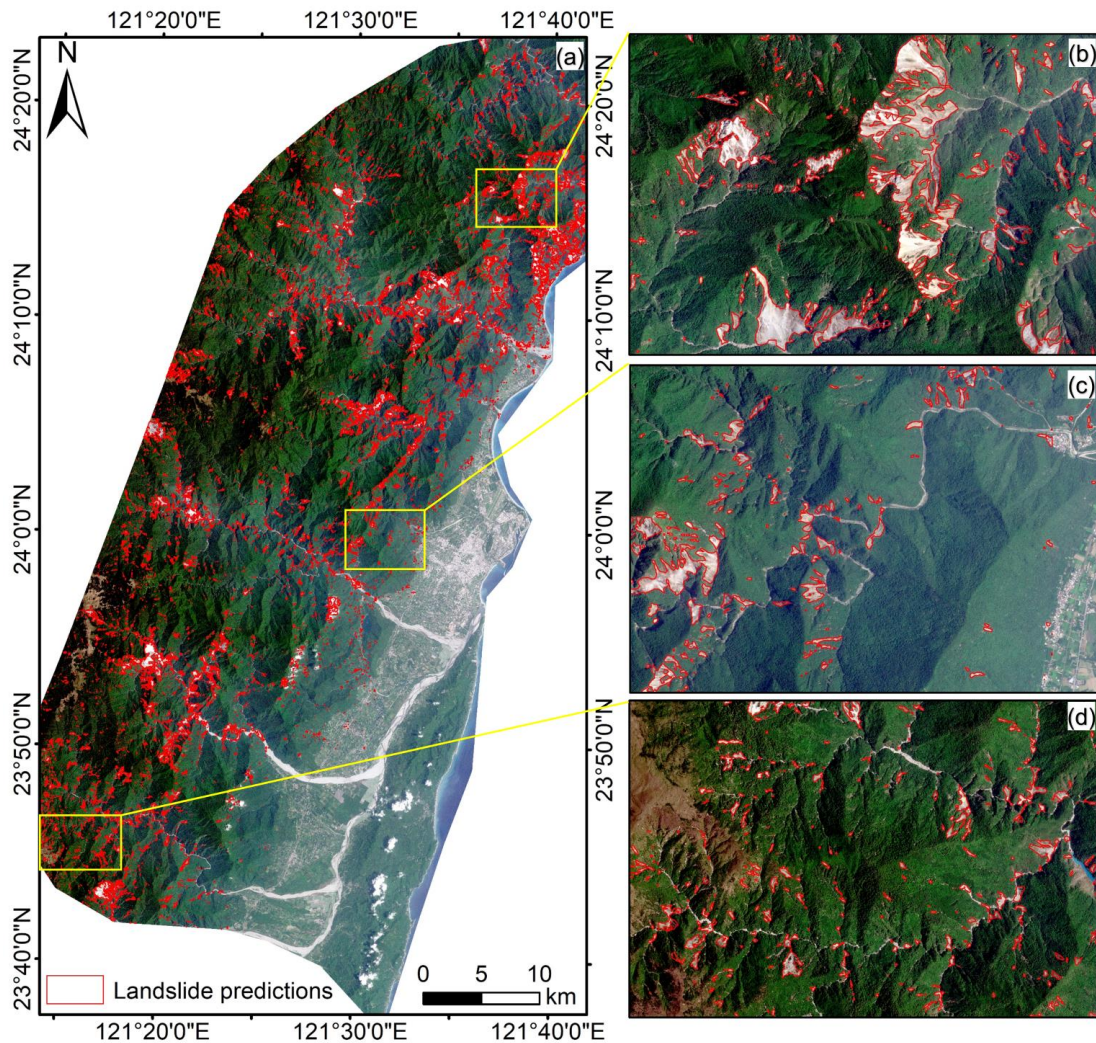
## 651 6.4 Practical Applications of GDCLD

652 To evaluate the practical applicability of the CDCLD, we selected two significant landslide-  
 653 triggering events that occurred in April 2024 for rapid landslide identification. These events  
 654 include landslides induced by a heavy rainfall in Meizhou, China and landslides triggered by an  
 655 earthquake in Hualien, China. In both cases, PlanetScope image was employed for

656 experimentation. For the Meizhou case, we obtained the image on May 14, 2024, and applied  
657 SegFormer model trained on GDCLD data to identify landslides triggered by the heavy rainfall.  
658 The results, shown in Figure.14, demonstrate that the GDCLD-trained model effectively  
659 mapped newly-induced landslides with a total area of 8.49 km<sup>2</sup>. The model exhibited excellent  
660 accuracy in avoiding false positives such as buildings, roads, and rivers. In terms of the Hualien  
661 event, we acquired post-event images from April 17 to 29, 2024. The rapid identification results,  
662 displayed in Figure.15, indicate that the GDCLD-trained model effectively eliminates false  
663 positives, such as roads, buildings, bare ground, and rivers, with the identified landslide area  
664 of 90.9 km<sup>2</sup>. The original PlanetScope images and landslide recognitions of the two events are  
665 available at <https://doi.org/10.5281/zenodo.13612636> (Fang et al., 2024)



666  
 667 **Figure.14** Detection results of rainfall-induced landslides for Meizhou, China. (a) is the aerial  
 668 view of the whole area, (b), (c) and (d) is the partial details. Map credits: PlanetScope.



669

670 **Figure.15** Detection results of earthquake-triggered landslides for Hualien, China. (a) is the  
 671 aerial view of the whole area, (b), (c) and (d) is the partial details. Map credits: PlanetScope.

## 672 7. Future research directions

673 The current GDCLD primarily comprises landslide samples from regions with significant  
 674 vegetation coverage, with limited representation from areas with low vegetation cover, such as  
 675 loess landslides. To address this, we have updated the database with high-resolution UAV data  
 676 (0.1m resolution) of loess landslides triggered by the  $M_w$  6.2 earthquake in Jishishan, Gansu,  
 677 China, in December 2023. Incorporating these loess landslide samples would enhance the  
 678 dataset's diversity and improve the generalization capability of landslide detection models.  
 679 Ongoing efforts to track and integrate data from landslides triggered by future extreme events

680 including strong earthquakes, heavy rainfall, and hurricanes, will further enrich the dataset.

681 In addition to expanding the GDCLD dataset, developing a large-scale vision model for  
682 landslide detection, such as a Segment Anything Model tailored for landslide identification and  
683 trained on GDCLD, is a crucial step forward in advancing AI-based landslide detection. This  
684 model will be used for the intelligent recognition of landslides in multi-source remote sensing  
685 image on a global scale.

686 Note that GDCLD is generally more applicable to semantic segmentation rather than  
687 instance segmentation for landslide identification task. Unlike other instance segmentation  
688 tasks, landslide segmentation presents unique challenges due to the frequent mixing of the  
689 "deposit" areas of adjacent landslide bodies (Hung et al., 2014). In most cases, we can only  
690 intuitively identify the "source" area of a landslide. This phenomenon is commonly observed in  
691 events such as the landslides triggered by the 2022 Luding earthquake in China (Figure.S10).  
692 Under these circumstances, it is often not feasible to separate individual landslides directly from  
693 2D optical images. Instead, it is necessary to consider the movement characteristics of each  
694 object from a 3D perspective (Bhuyan et al., 2024; Marc and Hovius, 2015) and combine this  
695 with topographic data to create accurate landslide labels for instance segmentation. However,  
696 generating such datasets requires high-resolution digital elevation models (DEM) and UAV or  
697 direct use of point cloud data. Given the global limitations in publicly available DEM (30m),  
698 achieving such fine distinctions is challenging. Therefore, our current study primarily focuses  
699 on semantic segmentation tasks. In future research, we plan to prepare landslide labels for  
700 instance segmentation based on LiDAR observation, and to develop specialized algorithms to  
701 address this complex issue.

## 702 **8. Code and data availability**

703 The data is freely available at <https://doi.org/10.5281/zenodo.13612636> (Fang et al., 2024).  
704 There are compressed folders, namely train\_dataset.zip, val\_dataset.zip and test\_dataset.zip.  
705 The train\_dataset.zip file contains 11,162 TIFF-format RGB images and their corresponding  
706 binary label data, with each image having dimensions of 1024×1024 pixels. The val\_dataset.zip



707 file comprises 4,459 TIFF-format RGB images and binary label data, with each image also  
708 sized at 1024×1024 pixels. The test\_data.zip file includes seven original remote sensing  
709 images from four landslide events, with images in TIFF-format RGB and labels in TIFF-format  
710 binary data, though the image dimensions vary. **The Future work folder contains some remote**  
711 **sensing data that will be added later.** For each label, "0" indicates the background, while "1"  
712 denotes the landslide. In addition, the other original data of UAV, Map World and Gaofen-6 are  
713 non-public data. **Both the Map World and GF-6 datasets were accessed under an image license**  
714 **acquired by our team. The UAV data are under the usage rights of the laboratory affiliated with**  
715 **our team. If you need to use them, please contact the corresponding author. The original**  
716 **PlanetScope data were obtained through the Planet Education and Research Program. You**  
717 **can get original imageries at <https://www.planet.com/> (Planet Team, 2019). And the code used**  
718 **to produce data described in this paper, as well as to create figures and tables, can be accessed**  
719 **at <https://github.com/PaddlePaddle/PaddleSeg>.**

## 720 9. Conclusion

721 Landslide mapping across extensive geographic areas using remote sensing proves to be  
722 a significant challenge. Although previous attempts have produced landslide datasets and  
723 advanced automation and intelligence, they have not been able to overcome limitations of  
724 specific events and data sources. In this research, we proposed the Globally Distributed  
725 Coseismic Landslide Dataset (GDCLD), an innovative resource crafted to autonomously and  
726 precisely tackle the intricacies of landslide mapping. We made **three** significant contributions in  
727 this work. Firstly, we meticulously interpreted multi-source remote sensing data to create a  
728 comprehensive dataset for landslide detection. This dataset contains  $1.39 \times 10^9$  annotated  
729 landslide pixels and remote sensing image at four different resolutions, spanning nine global  
730 regions. It successfully addresses the crucial lack of large-scale datasets in current landslide  
731 identification research. Secondly, we utilized GDCLD-trained model to showcase its robustness  
732 and generalization in landslide identification across diverse geographical contexts. Our  
733 proposed dataset shows a great potential in rapid response and emergency management of

734 geological hazards. Although the landslide samples are obtained from seismic events, the  
735 trained model enable to capture and learn the characteristic differences between landslides  
736 and the surroundings, making them suitable for landslide mapping beyond seismic-triggered  
737 events, such as those caused by rainfall. The comparative analyses with existing datasets  
738 highlight its effectiveness as the data base of deep learning model in mapping landslides across  
739 various global regions. **Finally, we demonstrate the superiority of the Transformer architecture  
740 over conventional CNN architecture in the task of landslide identification using multi-source  
741 remote sensing image. The GDCLD-S model further highlights the enhanced generalization  
742 capabilities of multi-source data compared to single-source data.** This work has great practical  
743 implications for prevention and mitigation of geological hazard worldwide.

## 744 Supplement

745 The supplement related to this article is available online at: XXXX

## 746 Author contributions

747 All the authors contributed equally to the preparation of the paper, from data curation to  
748 the review of the final paper.

## 749 Competing Interest

750 The authors declare that they have no known competing financial interests or personal  
751 relationships that could have appeared to influence the work reported in this paper.

752

## 753 Disclaimer

754 Publisher's note: Copernicus Publications remains neutral with regard to jurisdictional  
755 claims in published maps and institutional affiliations.

756

## 757 Acknowledgements

758 The research is supported by the National Science Fund for Distinguished Young Scholars  
759 of China (Grant No. 42125702), the National Natural Science Foundation of China (Grant No.  
760 42307263), the New Cornerstone Science Foundation through the XPLOER PRIZE (Grant  
761 No. XPLOER-2022-1012), the Natural Science Foundation of Sichuan Province (Grant No.  
762 2022NSFSC0003 and 2022NSFSC1083), and the China Scholarship Council (CSC NO.  
763 202409230002). We would like to thank the State Key Laboratory of Geohazard Prevention  
764 and Geoenvironment Protection for providing UAV data, the National Platform for Common  
765 GeoSpatial Information Services for MAP WORLD data, and the China Centre for Resources  
766 Satellite Data and Application for Gaofen-6 data. We would like to thank Kushanav Bhuyan for  
767 helping improve the English and general writing in this paper. We sincerely thank all colleagues  
768 who contributed to the landslide interpretation work. Finally, we sincerely thank the Anonymous  
769 Reviewers for their precious time and insightful comments, which are very helpful for us to  
770 improve the quality and readability of our manuscript.

## 771 Reference

- 772 Alpert, L.: Rainfall maps of Hispaniola, Bulletin of the American Meteorological Society, 423-  
773 431, 1942.
- 774 Basofi, A., Fariza, A., and Dzulkarnain, M. R.: Landslides susceptibility mapping using fuzzy  
775 logic: A case study in Ponorogo, East Java, Indonesia, 2016 International Conference on  
776 Data and Software Engineering (ICoDSE), 1-7,
- 777 Bhuyan, K., Rana, K., Ferrer, J. V., Cotton, F., Ozturk, U., Catani, F., and Malik, N.: Landslide  
778 topology uncovers failure movements, Nature communications, 15, 2633, 2024.
- 779 Bhuyan, K., Tanyaş, H., Nava, L., Puliero, S., Meena, S. R., Floris, M., Van Westen, C., and  
780 Catani, F.: Generating multi-temporal landslide inventories through a general deep transfer  
781 learning strategy using HR EO data, Scientific reports, 13, 162, 2023.
- 782 Brardinoni, F., Slaymaker, O., and Hassan, M. A.: Landslide inventory in a rugged forested  
783 watershed: a comparison between air-photo and field survey data, Geomorphology, 54,  
784 179-196, 2003.
- 785 Burrows, K., Walters, R. J., Milledge, D., Spaans, K., and Densmore, A. L.: A new method for  
786 large-scale landslide classification from satellite radar, Remote Sensing, 11, 237, 2019.
- 787 Calais, E., Symithe, S., Monfret, T., Delouis, B., Lomax, A., Courboulex, F., Ampuero, J. P., Lara,  
788 P. E., Bletery, Q., Cheze, J., Peix, F., Deschamps, A., de Lepinay, B., Raimbault, B., Jolivet,

789 R., Paul, S., St Fleur, S., Boisson, D., Fukushima, Y., Duputel, Z., Xu, L., and Meng, L.:  
790 Citizen seismology helps decipher the 2021 Haiti earthquake, *Science*, 376, 283-287,  
791 10.1126/science.abn1045, 2022.

792 Cao, H., Wang, Y., Chen, J., Jiang, D., Zhang, X., Tian, Q., and Wang, M.: Swin-unet: Unet-like  
793 pure transformer for medical image segmentation, *European conference on computer  
794 vision*, 205-218,

795 Casagli, N., Intrieri, E., Tofani, V., Gigli, G., and Raspini, F.: Landslide detection, monitoring and  
796 prediction with remote-sensing techniques, *Nature Reviews Earth & Environment*, 4, 51-  
797 64, 2023.

798 Chau, K. T., Sze, Y., Fung, M., Wong, W., Fong, E., and Chan, L.: Landslide hazard analysis  
799 for Hong Kong using landslide inventory and GIS, *Computers & Geosciences*, 30, 429-443,  
800 2004.

801 Chen, B., Xu, B., Zhu, Z., Yuan, C., Suen, H. P., Guo, J., Xu, N., Li, W., Zhao, Y., and Yang, J.:  
802 Stable classification with limited sample: Transferring a 30-m resolution sample set  
803 collected in 2015 to mapping 10-m resolution global land cover in 2017, *Sci. Bull*, 64, 3,  
804 2019.

805 Chicco, D. and Jurman, G.: The advantages of the Matthews correlation coefficient (MCC) over  
806 F1 score and accuracy in binary classification evaluation, *BMC Genomics*, 21, 6,  
807 10.1186/s12864-019-6413-7, 2020.

808 Cigna, F., Tapete, D., and Lee, K.: Geological hazards in the UNESCO World Heritage sites of  
809 the UK: From the global to the local scale perspective, *Earth-Science Reviews*, 176, 166-  
810 194, 2018.

811 Cigna, F., Osmanoglu, B., Cabral-Cano, E., Dixon, T. H., Ávila-Olivera, J. A., Garduño-Monroy,  
812 V. H., DeMets, C., and Wdowinski, S.: Monitoring land subsidence and its induced  
813 geological hazard with Synthetic Aperture Radar Interferometry: A case study in Morelia,  
814 Mexico, *Remote Sensing of Environment*, 117, 146-161, 2012.

815 Coe, J. A., Ellis, W. L., Godt, J. W., Savage, W. Z., Savage, J. E., Michael, J., Kibler, J. D.,  
816 Powers, P. S., Lidke, D. J., and Debray, S.: Seasonal movement of the Slumgullion  
817 landslide determined from Global Positioning System surveys and field instrumentation,  
818 July 1998–March 2002, *Engineering geology*, 68, 67-101, 2003.

819 Dai, L., Fan, X., Wang, X., Fang, C., Zou, C., Tang, X., Wei, Z., Xia, M., Wang, D., and Xu, Q.:  
820 Coseismic landslides triggered by the 2022 Luding Ms6. 8 earthquake, China, *Landslides*,  
821 20, 1277-1292, 2023.

822 De Boer, P.-T., Kroese, D. P., Mannor, S., and Rubinstein, R. Y.: A tutorial on the cross-entropy  
823 method, *Annals of operations research*, 134, 19-67, 2005.

824 Diakogiannis, F. I., Waldner, F., Caccetta, P., and Wu, C.: ResUNet-a: A deep learning  
825 framework for semantic segmentation of remotely sensed data, *ISPRS Journal of  
826 Photogrammetry and Remote Sensing*, 162, 94-114, 2020.

827 Fan, X., Scaringi, G., Xu, Q., Zhan, W., Dai, L., Li, Y., Pei, X., Yang, Q., and Huang, R.:  
828 Coseismic landslides triggered by the 8th August 2017 M s 7.0 Jiuzhaigou earthquake  
829 (Sichuan, China): factors controlling their spatial distribution and implications for the  
830 seismogenic blind fault identification, *Landslides*, 15, 967-983, 2018.

831 Fang, C., Fan, X., & Wang, X. (2024). GDCLD:A globally distributed dataset of coseismic  
832 landslide mapping via multi-source high-resolution remote sensing images [Data set].  
833 Zenodo. <https://doi.org/10.5281/zenodo.13612636>.

834 Fang, C., Fan, X., Zhong, H., Lombardo, L., Tanyas, H., and Wang, X.: A Novel historical  
835 landslide detection approach based on LiDAR and lightweight attention U-Net, *Remote*  
836 *Sensing*, 14, 4357, 2022.

837 Fiorucci, F., Ardizzone, F., Mondini, A. C., Viero, A., and Guzzetti, F.: Visual interpretation of  
838 stereoscopic NDVI satellite images to map rainfall-induced landslides, *Landslides*, 16, 165-  
839 174, 2019.

840 Fiorucci, F., Cardinali, M., Carlà, R., Rossi, M., Mondini, A., Santurri, L., Ardizzone, F., and  
841 Guzzetti, F.: Seasonal landslide mapping and estimation of landslide mobilization rates  
842 using aerial and satellite images, *Geomorphology*, 129, 59-70, 2011.

843 Gao, H., Yin, Y., Li, B., Gao, Y., Zhang, T., Liu, X., and Wan, J.: Geomorphic evolution of the  
844 Sedongpu Basin after catastrophic ice and rock avalanches triggered by the 2017 Ms6. 9  
845 Milin earthquake in the Yarlung Zangbo River area, China, *Landslides*, 1-15, 2023.

846 Gao, J. and Maro, J.: Topographic controls on evolution of shallow landslides in pastoral  
847 Wairarapa, New Zealand, 1979–2003, *Geomorphology*, 114, 373-381, 2010.

848 Ghorbanzadeh, O., Xu, Y., Zhao, H., Wang, J., Zhong, Y., Zhao, D., Zang, Q., Wang, S., Zhang,  
849 F., and Shi, Y.: The outcome of the 2022 landslide4sense competition: Advanced landslide  
850 detection from multisource satellite imagery, *IEEE Journal of Selected Topics in Applied*  
851 *Earth Observations and Remote Sensing*, 15, 9927-9942, 2022.

852 Gorum, T., Fan, X., van Westen, C. J., Huang, R. Q., Xu, Q., Tang, C., and Wang, G.:  
853 Distribution pattern of earthquake-induced landslides triggered by the 12 May 2008  
854 Wenchuan earthquake, *Geomorphology*, 133, 152-167, 2011.

855 Guzzetti, F., Mondini, A. C., Cardinali, M., Fiorucci, F., Santangelo, M., and Chang, K.-T.:  
856 Landslide inventory maps: New tools for an old problem, *Earth-Science Reviews*, 112, 42-  
857 66, 2012.

858 Harp, E. L., Jibson, R. W., and Schmitt, R. G.: Map of landslides triggered by the January 12,  
859 2010, Haiti earthquake, US Geological Survey Scientific Investigations Map, 3353, 15,  
860 2016.

861 He, K., Zhang, X., Ren, S., and Sun, J.: Deep residual learning for image recognition,  
862 *Proceedings of the IEEE conference on computer vision and pattern recognition*, 770-778,

863 Hu, K., Zhang, X., You, Y., Hu, X., Liu, W., and Li, Y.: Landslides and dammed lakes triggered  
864 by the 2017 Ms6. 9 Milin earthquake in the Tsangpo gorge, *Landslides*, 16, 993-1001, 2019.

865 Huang, R. and Fan, X.: The landslide story, *Nature Geoscience*, 6, 325-326, 2013.

866 Huang, R., Pei, X., Fan, X., Zhang, W., Li, S., and Li, B.: The characteristics and failure  
867 mechanism of the largest landslide triggered by the Wenchuan earthquake, May 12, 2008,  
868 China, *Landslides*, 9, 131-142, 2012.

869 Huang, Y., Xu, C., Zhang, X., Xue, C., and Wang, S.: An Updated Database and Spatial  
870 Distribution of Landslides Triggered by the Milin, Tibet M w6. 4 Earthquake of 18 November  
871 2017, *Journal of Earth Science*, 32, 1069-1078, 2021.

872 Hungr, O., Leroueil, S., and Picarelli, L.: The Varnes classification of landslide types, an update,

873 Landslides, 11, 167-194, 2014.

874 Ji, S., Yu, D., Shen, C., Li, W., and Xu, Q.: Landslide detection from an open satellite imagery  
875 and digital elevation model dataset using attention boosted convolutional neural networks,  
876 Landslides, 17, 1337-1352, 2020.

877 Li, Z., Shi, W., Lu, P., Yan, L., Wang, Q., and Miao, Z.: Landslide mapping from aerial  
878 photographs using change detection-based Markov random field, Remote sensing of  
879 environment, 187, 76-90, 2016.

880 Li, Z., Shi, A., Li, X., Dou, J., Li, S., Chen, T., and Chen, T.: Deep learning-based landslide  
881 recognition incorporating deformation characteristics, Remote Sensing, 16, 992, 2024.

882 Liu, J., Huang, X., Song, G., Li, H., and Liu, Y.: Uninet: Unified architecture search with  
883 convolution, transformer, and mlp, European Conference on Computer Vision, 33-49,

884 Liu, Z., Lin, Y., Cao, Y., Hu, H., Wei, Y., Zhang, Z., Lin, S., and Guo, B.: Swin transformer:  
885 Hierarchical vision transformer using shifted windows, Proceedings of the IEEE/CVF  
886 international conference on computer vision, 10012-10022,

887 Loshchilov, I. and Hutter, F.: Decoupled weight decay regularization, arXiv preprint  
888 arXiv:1711.05101, 2017.

889 Lu, P., Qin, Y., Li, Z., Mondini, A. C., and Casagli, N.: Landslide mapping from multi-sensor data  
890 through improved change detection-based Markov random field, Remote Sensing of  
891 Environment, 231, 111235, 2019.

892 Luppino, L. T., Hansen, M. A., Kampffmeyer, M., Bianchi, F. M., Moser, G., Jenssen, R., and  
893 Anfinsen, S. N.: Code-Aligned Autoencoders for Unsupervised Change Detection in  
894 Multimodal Remote Sensing Images, IEEE Trans Neural Netw Learn Syst, PP,  
895 10.1109/TNNLS.2022.3172183, 2022.

896 Ma, Y., Yu, D., Wu, T., and Wang, H.: PaddlePaddle: An open-source deep learning platform  
897 from industrial practice, Frontiers of Data and Computing, 1, 105-115, 2019.

898 Marc, O. and Hovius, N.: Amalgamation in landslide maps: effects and automatic detection,  
899 Natural Hazards and Earth System Science, 15, 723-733, 2015

900 Meena, S. R., Ghorbanzadeh, O., van Westen, C. J., Nachappa, T. G., Blaschke, T., Singh, R.  
901 P., and Sarkar, R.: Rapid mapping of landslides in the Western Ghats (India) triggered by  
902 2018 extreme monsoon rainfall using a deep learning approach, Landslides, 18, 1937-  
903 1950, 2021.

904 Meena, S. R., Nava, L., Bhuyan, K., Puliero, S., Soares, L. P., Dias, H. C., Floris, M., and Catani,  
905 F.: HR-GLDD: A globally distributed dataset using generalized DL for rapid landslide  
906 mapping on HR satellite imagery, Earth System Science Data Discussions, 1-21, 2022.

907 Metternicht, G., Hurni, L., and Gogu, R.: Remote sensing of landslides: An analysis of the  
908 potential contribution to geo-spatial systems for hazard assessment in mountainous  
909 environments, Remote sensing of Environment, 98, 284-303, 2005.

910 Mohan, A., Singh, A. K., Kumar, B., and Dwivedi, R.: Review on remote sensing methods for  
911 landslide detection using machine and deep learning, Transactions on Emerging  
912 Telecommunications Technologies, 32, e3998, 2021.

913 Mondini, A. C., Guzzetti, F., Chang, K.-T., Monserrat, O., Martha, T. R., and Manconi, A.:  
914 Landslide failures detection and mapping using Synthetic Aperture Radar: Past, present

915 and future, *Earth-Science Reviews*, 216, 103574, 2021.

916 Nava, L., Monserrat, O., and Catani, F.: Improving landslide detection on SAR data through  
917 deep learning, *IEEE Geoscience and Remote Sensing Letters*, 19, 1-5, 2021.

918 O'Shea, K. and Nash, R.: An introduction to convolutional neural networks, arXiv preprint  
919 arXiv:1511.08458, 2015.

920 Poveda, E., Pedraza, P., Velandia, F., Mayorga, E., Plicka, V., Gallovič, F., and Zahradník, J.:  
921 2019 Mw 6.0 Mesetas (Colombia) Earthquake Sequence: Insights From Integrating  
922 Seismic and Morphostructural Observations, *Earth and Space Science*, 9,  
923 e2022EA002465, 2022.

924 Rezatofighi, H., Tsoi, N., Gwak, J., Sadeghian, A., Reid, I., and Savarese, S.: Generalized  
925 intersection over union: A metric and a loss for bounding box regression, *Proceedings of  
926 the IEEE/CVF conference on computer vision and pattern recognition*, 658-666,

927 Ronneberger, O., Fischer, P., and Brox, T.: U-net: Convolutional networks for biomedical image  
928 segmentation, *Medical Image Computing and Computer-Assisted Intervention—MICCAI  
929 2015: 18th International Conference, Munich, Germany, October 5-9, 2015, Proceedings,  
930 Part III* 18, 234-241,

931 Shao, X., Ma, S., and Xu, C.: Distribution and characteristics of shallow landslides triggered by  
932 the 2018 Mw 7.5 Palu earthquake, Indonesia, *Landslides*, 20, 157-175, 2023.

933 Soares, L. P., Dias, H. C., Garcia, G. P. B., and Grohmann, C. H.: Landslide segmentation with  
934 deep learning: Evaluating model generalization in rainfall-induced landslides in Brazil,  
935 *Remote Sensing*, 14, 2237, 2022.

936 SS, V. C. and Shaji, E.: Landslide identification using machine learning techniques: Review,  
937 motivation, and future prospects, *Earth science informatics*, 15, 2063-2090, 2022.

938 Tang, D., Ge, W., and Cao, X.: Stress triggering of the 2022 Lushan–Maerkang earthquake  
939 sequence by historical events and its implication for fault stress evolution in eastern Tibet,  
940 *Frontiers in Earth Science*, 11, 1105394, 2023.

941 Townsend, J. T.: Theoretical analysis of an alphabetic confusion matrix, *Perception &  
942 Psychophysics*, 9, 40-50, 1971.

943 Udin, W., Norazami, N., Sulaiman, N., Zaudin, N. C., Ma'ail, S., and Nor, A. M.: UAV based  
944 multi-spectral imaging system for mapping landslide risk area along Jeli-Gerik highway,  
945 Jeli, Kelantan, 2019 *IEEE 15th International Colloquium on Signal Processing & Its  
946 Applications (CSPA)*, 162-167,

947 Valagussa, A., Marc, O., Frattini, P., and Crosta, G. B.: Seismic and geological controls on  
948 earthquake-induced landslide size, *Earth and Planetary Science Letters*, 506, 268-281,  
949 2019.

950 Wang, F., Fan, X., Yunus, A. P., Siva Subramanian, S., Alonso-Rodriguez, A., Dai, L., Xu, Q.,  
951 and Huang, R.: Coseismic landslides triggered by the 2018 Hokkaido, Japan (M w 6.6),  
952 earthquake: spatial distribution, controlling factors, and possible failure mechanism,  
953 *Landslides*, 16, 1551-1566, 2019.

954 Wang, J., Sun, K., Cheng, T., Jiang, B., Deng, C., Zhao, Y., Liu, D., Mu, Y., Tan, M., and Wang,  
955 X.: Deep high-resolution representation learning for visual recognition, *IEEE transactions  
956 on pattern analysis and machine intelligence*, 43, 3349-3364, 2020.

957 Xiao, T., Liu, Y., Zhou, B., Jiang, Y., and Sun, J.: Unified perceptual parsing for scene  
958 understanding, Proceedings of the European conference on computer vision (ECCV), 418-  
959 434,  
960 Xie, E., Wang, W., Yu, Z., Anandkumar, A., Alvarez, J. M., and Luo, P.: SegFormer: Simple and  
961 efficient design for semantic segmentation with transformers, Advances in Neural  
962 Information Processing Systems, 34, 12077-12090, 2021.  
963 Xu, Y., Ouyang, C., Xu, Q., Wang, D., Zhao, B., and Luo, Y.: CAS Landslide Dataset: A Large-  
964 Scale and Multisensor Dataset for Deep Learning-Based Landslide Detection, Sci Data,  
965 11, 12, 10.1038/s41597-023-02847-z, 2024.  
966 Yamagishi, H. and Yamazaki, F.: Landslides by the 2018 hokkaido iburi-tobu earthquake on  
967 september 6, Landslides, 15, 2521-2524, 2018.  
968 Yang, Z., Xu, C., and Li, L.: Landslide detection based on ResU-net with transformer and CBAM  
969 embedded: two examples with geologically different environments, Remote Sensing, 14,  
970 2885, 2022a.  
971 Yang, Z., Dai, D., Zhang, Y., Zhang, X., and Liu, J.: Rupture process and aftershock  
972 mechanisms of the 2022 Luding M6. 8 earthquake in Sichuan, China, Earthquake Science,  
973 35, 1-2, 2022b.  
974 Ye, C., Li, Y., Cui, P., Liang, L., Pirasteh, S., Marcato, J., Goncalves, W. N., and Li, J.: Landslide  
975 detection of hyperspectral remote sensing data based on deep learning with constrains,  
976 IEEE Journal of Selected Topics in Applied Earth Observations and Remote Sensing, 12,  
977 5047-5060, 2019.  
978 Yi, Y., Zhang, Z., Zhang, W., Jia, H., and Zhang, J.: Landslide susceptibility mapping using  
979 multiscale sampling strategy and convolutional neural network: A case study in Jiuzhaigou  
980 region, Catena, 195, 104851, 2020.  
981 Zhang, X., Yu, W., Pun, M.-O., and Shi, W.: Cross-domain landslide mapping from large-scale  
982 remote sensing images using prototype-guided domain-aware progressive representation  
983 learning, ISPRS Journal of Photogrammetry and Remote Sensing, 197, 1-17, 2023.  
984 Zhao, B., Li, W., Su, L., Wang, Y., and Wu, H.: Insights into the landslides triggered by the 2022  
985 Lushan Ms 6.1 earthquake: spatial distribution and controls, Remote Sensing, 14, 4365,  
986 2022a.  
987 Zhao, B., Wang, Y., Li, W., Lu, H., and Li, Z.: Evaluation of factors controlling the spatial and  
988 size distributions of landslides, 2021 Nippes earthquake, Haiti, Geomorphology, 415,  
989 108419, 2022b.  
990 Zhong, C., Liu, Y., Gao, P., Chen, W., Li, H., Hou, Y., Nuremanguli, T., and Ma, H.: Landslide  
991 mapping with remote sensing: challenges and opportunities, International Journal of  
992 Remote Sensing, 41, 1555-1581, 2020.

993